CO$_2$ COOLING STUDIES FOR THE ATLAS UPGRADE

Author:
Gijs HEMINK, BSc
Univ. of Twente/NIKHEF
Faculty of Science and Technology
Applied Physics, ATLAS group

· · · · · · · · · · · ·

Internship at:

· · · · · · · · · · · ·

Direct Supervisor:
Marco Oriunno, Dr.
SLAC National Accelerator Laboratory
Senior Research Engineer

Supervisor University of Twente:
Bob van Eijk, Prof. Dr. Ing.
NIKHEF National Institute for Subatomic Physics
ATLAS department

JUNE, 2010

Abstract

This thesis focusses on the advanced cooling issues for the ATLAS upgrade. Describing the thermal measurements done to assess the possible use of evaporative carbon dioxide as refrigerant. It has been investigated how CO_2 behaves inside small diameter tubes under different evaporation temperatures and different mass fluxes, centralized around the design properties of the phased upgrade for ATLAS and focussed on the heat transfer coefficient of CO_2. Furthermore, the thermal impedance of the first prototype for the IBL upgrade has been determined. To accomplish these goals, the blown system and corresponding data acquisition system at SLAC National Laboratory have been improved to increase the reliability, handle the data better, and make it work faster. The results show a clear agreement with the theoretical predictions, furthermore it is concluded that CO_2 would be an excellent coolant for the ATLAS phased upgrades.

Contents

G Wires **78**

Chapter 1

Introduction

1.1 Large Hadron Collider

The Large Hadron Collider (LHC) is the world's largest and highest-energy particle accelerator. It is built by the European Organization for Nuclear Research (CERN) to collide opposing proton particle beams at an energy of 7 trillion electron volts (TeV) to test various predictions of high-energy physics, including the existence of the hypothesized Higgs boson and of the large family of new particles predicted by supersymmetry.

LHC is a truly large scale project, lying in a 27 kilometers circumference circular tunnel, as much as 175 meters beneath the Franco-Swiss border near Geneva, Switzerland and being funded by and built in collaboration with over 10,000 scientists and engineers from over 100 countries as well as hundreds of universities and laboratories [1]. The LHC operation started on September 2008 with low energy beams of 450 GeV and in 2010 the beams where finally ramped up 3.5 TeV, half its designed energy. There the first collision took place, surpassing the world record of 1.18 TeV previously held by the Tevatron at Fermilab [2, 3].

Six particle detectors have been constructed at the LHC to observe the particles that are produced at the four collision points. Two of them, A Toroidal LHC ApparatuS, better known as ATLAS, and the Compact Muon Solenoid (CMS), are large, general purpose particle detectors. A Large Ion Collider Experiment (ALICE) and LHCb have more specific roles and the last two, TOTEM and LHCf, are smaller and are constructed for specialized research.

1.2 ATLAS detector

ATLAS is the largest detector ever built at a particle collider. Its purpose is to probe the Standard Model by detecting and studying the decay of the particles produced at the interaction point. One of the most important goals of ATLAS is to investigate a missing piece of the Standard Model, the Higgs boson, which would be eventually highlighted by the decay of a specific combination of quarks and leptons. Furthermore it is investigating CP violation and super symmetry [4].

Dedicated sub-detectors with a large variety of technologies, as is depicted in Figure 1.1, are embedded in magnetic fields to measure charge, energy, mass and momentum of decay products. ATLAS contains six sub-detectors with two

superconductive magnetic systems: a two Tesla solenoid surrounding the inner detector, a set of eight large toroids all situated outside the calorimeters and within the muon system.
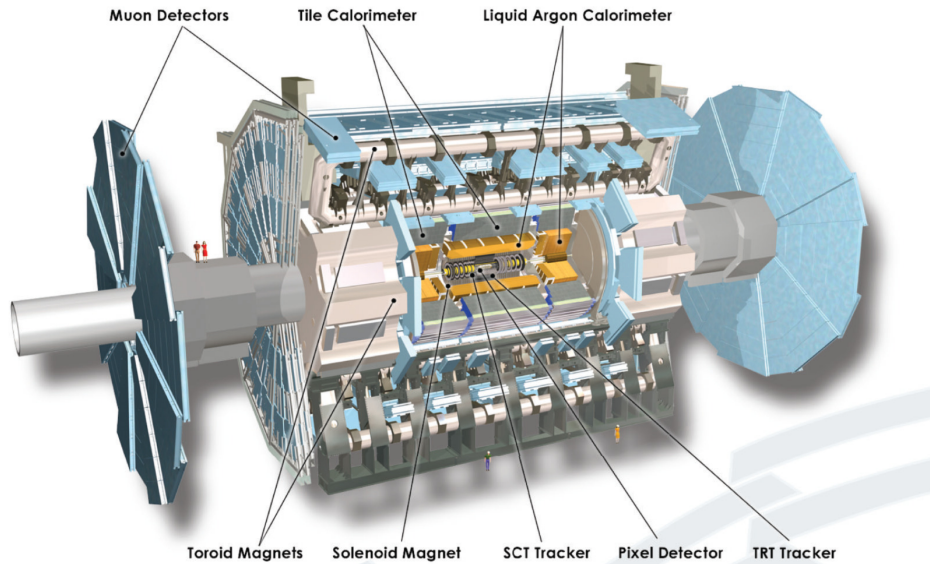
Figure 1.1: ATLAS experiment with the main detectors. From beam to the outside: vertex detector, SCT tracker, TRT tracker, Liquid Argon Calorimeter, Tile Calorimeter and the Muon detectors. (courtesy of "The ATLAS experiment at CERN, http://atlas.ch")

Inner detector

Closest to the beam pipe are the Vertex (pixel detector), the Inner Detector (SCT) and the Transition Radiation Tracker (TRT), with planar silicon pixels, silicon strip and gas drift tube technology respectively. They measure the charge and the momentum by the bending of the particle tracks in the two Tesla magnetic field.

Calorimeters

The energy of leptons and hadrons is measured with the Electromagnetic and the Hadronic calorimeters, respectively. The electromagnetic calorimeter is inside a cryostat and cooled with liquid Argon at $87\ °$K with lead and stainless steel as sampling material. The Hadronic calorimeter operates at room temperature detecting hadrons, mesons, and other particles that interact through the strong force. It consists out of stainless steel sampling material and uses scintillating tiles as detecting elements, resulting in a high energy resolution.

Muon detectors

Finally, the heavy brother of the electron, the muon is detected at the larger radius in the muon detector, which is made of gas resistive plate chambers and placed

inside the outer toroidal magnetic field system. Eight large air-core supercon-
ducting barrel loops and two end-cap modules produces a 25.3 meters long and
20.1 meters in diameter wide magnetic field, storing 1.08 giga joules of energy [4].
The muon's low interaction with the previous described sub-detectors means that
it would leave the detector unnoticed if these detectors would be absent. This
would compromise the measurement of the total deposited energy. Furthermore,
the muon plays a roll in a number of interesting physical processes (e.g. $H \to ZZ^*$
$\to l^+ l^- l^+ l^-$ where a Higgs bosons decays to two Z bosons, which will subse-
quently decay to $e^- e^+$ or $\mu^- \mu^+$ [4]).

Measurements

Measurements of one of the first collisions in ATLAS at 3.5 TeV provides a clear
view of how the complete sub-detectors work together to reconstruct an event.
This is shown in Figure 1.2.
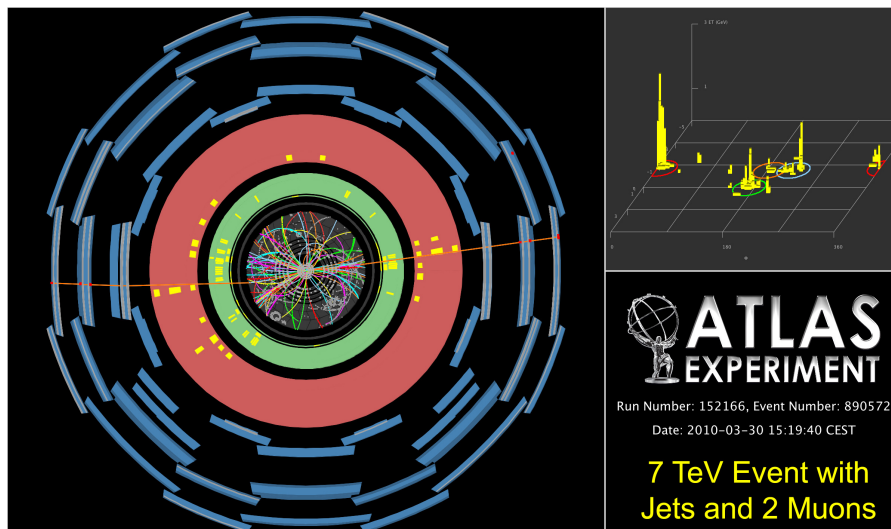
Figure 1.2: Candidate Z decays to leptons at 7 TeV centre-of-mass energy in the
ATLAS detector: 2010-03-30. (courtesy of "The ATLAS experiment at CERN,
http://atlas.ch")

1.3   Phased upgrades

Development of technology continues, so while the LHC has started, there are
already plans for phased upgrades of the machine hardware. The goal is to in-
crease, in steps, the luminosity and consequently the potential of scientific discov-
ery. The proton density will be higher and more collisions will take place. The
sub-detectors closest to the collision point will be required to stand higher radi-
ation doses, and has to use low density materials to be effective in the higher
particle background.

Phase I

For the Phase I upgrade, ATLAS has the goal to restore the tracking efficiency that is lost by the detectors getting irradiated once the machine reaches the luminosity of 10^{34} cm^{-2} s^{-1} [4]. This can be accomplished by adding a new layer of pixel sensors mounted on a reduced ($29 \rightarrow 25$ mm [5]) beam pipe [6].

Phase II

For the upgrade Phase II the full Inner Tracker needs to be replaced to stand the even more demanding environment due to the high luminosity of 10^{35} cm^{-2} s^{-1}.

R&D

For both phases, research area where intense R&D programs have started are: radiation hard pixels, lightweight local supports and advanced cooling.

1.3.1 Radiation hard Pixel sensors

Three options are proposed: planar silicon, diamond and 3D silicon [6]. The first is used in the current pixel detector, has very well understood manufacturing sources, offers a high yield at a relatively low cost, but operates at high voltage and degenerates rapidly due to radiation in comparison with the other two options.

   Diamond could be a better option because it needs the least cooling and has low noise while operating. However, manufacturing them with high yield for a low cost still has to be shown.

   3D silicon sensors seem also to be a good alternative, if it can be shown that it is possible to make them with high yield and good uniformity. However, studies for all three sensors are still in progress and decisions still have to be made [6].

1.3.2 Local supports

Lightweight local support with low density, high stability and high thermal conductivity for the pixel sensors is required to minimize the amount of material that can create multiple scattering, providing at the same time adequate cooling performances. New materials like carbon foams are studied with interests and some full scale prototypes are being produced and tested [7].

1.3.3 Advanced Cooling

The heat load produced by the front end electronics and the increased leakage current on the sensor due to the high irradiation, require high thermal efficiency and lower temperature to prevent thermal runaway. Moreover, reducing materials, low pressure drop and temperature uniformity along sensors must also be guaranteed.

   The present ATLAS Tracker detector is refrigerated by an evaporative flow of octafluoropropane (R218, C_3F_8). Such fluid has generally shown good performance for similar applications [8, 9]. However, it has limitations for use in future detectors because of the low or even sub-atmospheric saturation pressure at

the temperatures of interest (-40 °C, -35 °C), and the high pressure drops in small diameter tubes. This limits the potential mass reductions of the structures. Therefore, ATLAS is looking for an alternative refrigerant that is able to provide low evaporation temperatures around -35 °C [7]. This is especially important for innermost Pixel layers, which have the highest risk of thermal runaway.

1.4   Coolant

Among the refrigerants under consideration is Carbon Dioxide (R744, CO_2), which shows excellent properties, in addition it is a cheap and a natural gas. Besides the great advantage of negligible Global Warming Potential and impact on the ozone layer, it is a dielectric fluid that is not toxic, not flammable and not corrosive. Moreover, it has a high chemical stability under irradiation, which is a necessity for applications involving particle accelerators.

The two-phase flow characteristics of CO2 are quite different from those of other refrigerants, because of the high pressure in operation, the higher vapor density, the lower surface tension, the lower liquid viscosity and the higher vapor viscosity. High pressures and low surface tensions are responsible for the clear dominance of nucleate boiling heat transfer, with values higher than those of conventional refrigerants at the same saturation temperature. In addition, at high mass velocities, dry out may occur at moderate vapor quality. Of special interest for applications requiring mass reduction, such as ATLAS, is the possibility to combine the effects of the high pressure and the higher heat transfer coefficient to reduce the diameter—hence, mass—of the cooling channel and the refrigerants volume.

CO2 has already been used with success to refrigerate scientific instruments, such as the space experiment AMS [10], where reliability and low mass requirements are crucial, and for the vertex detector VELO [11] at LHC, in a vacuum vessel at few millimeters from the interaction point, where radiation hardness must also be considered.

The main characteristics of CO2 are:

1. Abundant in nature/cheap

2. Not toxic

3. Not flammable

4. Low triple point at high pressure (-56 °C, 5.6 bar)

5. Low critical point at high pressure (31 °C, 76 bar)

6. High vapor pressure curve (4 to 10 times C_3F_8)

7. Low temperature drop due to low pressure drop at the saturation temperatures

8. Low viscosity

9. High latent heat

10. High heat transfer coefficient

Among all the other properties, those which make carbon dioxide especially attractive for the ATLAS Inner Detector cooling system are its low triple point at still high pressure and the high refrigeration capacity. The first allows to reach the required lower evaporation temperatures. The high refrigeration capacity means an efficient heat absorption by using smaller tubes, thus reducing materials. The high pressure in the pipes (ranging between 10 to 60 bar), provides advantages like an easier achievement of lower temperatures. Furthermore, the low viscosities of the gas and liquid phase mean for two-phase flow a small pressure drop along tubes; resulting in a low temperature gradient along the pixel sensors.

New research

Although the study on CO_2 increases , still much should be investigated and documented. There is especially a lack of information concerning the heat transfer coefficient in micro-channels and small diameter tubes at evaporation temperatures below 0 °C. This information is vital to determine if CO_2 can be used as coolant, because the fluid has to be capable of evacuating more then 6 kW/m^2 of produced heat.

1.5   Focus

This thesis focusses therefore on the advanced cooling issues for the ATLAS upgrade describing the thermal measurements done to assess the possible use of evaporative carbon dioxide as refrigerant. It will investigate how CO_2 behaves inside small diameter tubes under different evaporation temperatures and different mass fluxes, centralized around the design properties of the phased upgrade for ATLAS and focussed on the heat transfer coefficient of CO_2. Furthermore, the thermal impedance of the first prototypes staves for the IBL upgrade will be determined. To accomplish these goals, the blown system and corresponding data acquisition system at SLAC National Laboratory has to be improved to make it work faster, handle the data better, and to increase the reliability.

1.6   Thesis outline

In chapter 2 more details for the detector upgrades are presented followed by theoretical models of heat convection. chapter 3 explains the experimental setup and the blown systems improvements that have been made. It also presents the renewed data acquisition system which contains a Labview program that is responsible for data taking and a Matlab program that is capable of processing the data, calculates all the wanted quantities, and furthermore compares the results with the available theoretical models [12, 13] for CO_2. Subsequently, the results are presented in chapter 4. Finally, the deduced conclusions are presented in chapter 5, and details about further investigation are introduced.

Chapter 2

Theory

2.1 Cooling requirements

2.1.1 Thermal runaway

Semiconductor based detectors, particularly Pixels, need to be cooled to evacuate the heat produced by the Front End electronic to reduce the noise due to leakage current and to provide stable operation conditions against the so called thermal runaway.

The power P_{Si} dissipated by a silicon detector itself is given by the product of bias voltage U_{bias} and leakage current I_{leak} [14].

$$P_{Si} = U_{bias} \cdot I_{leak} \qquad (2.1)$$

The bias voltage has to be much higher than the depletion voltage U_{dep} to guarantee satisfactory detector operation. This may reach over hundreds of volts after a few years of LHC operation due to type inversion and reverse annealing. Fortunately, the latter can be avoided if the silicon detectors are always kept below 0 °C, this sets the first upper limit for cooling. This requirement also has to be ensured when the experiment is shutdown for repair work. The leakage current increases with radiation dose because of radiation damage formed mostly due to bulk damage in silicon. The total power dissipation of a radiated silicon sensor can be approximated by using Boltzmann statistics, as presented in Equation 2.2 [14].

$$P_{Si}(T, U_{bias}) \approx U_{bias} \cdot \kappa \cdot \Phi \cdot V \cdot T^2 \cdot \exp \frac{-7020.7K}{T} \qquad (2.2)$$

where κ is called the leakage current damage constant $[A/m]$ ($\kappa \approx 3.5 \cdot 10^{-15} A/m$ at 20°C [14]), Φ is the particle fluence $[1/m^2]$ to which the detector has been irradiated, V is the silicon sensor volume, $k = 8.62 \cdot 10^{-5} \ [eV/°K]$ being Boltzmanns constant and T the temperature of the silicon $[°K]$. In the temperature range of interest this means that the leakage current doubles every 7 °C.

Any cooling system based on fluid convection, leads to a linear increase of the silicon temperature with the power dissipated in the silicon, Equation 2.3 [14]:

$$\Delta T = T_{Si} - T_f = \frac{P_{Si}}{h \cdot A} \qquad (2.3)$$

where h is the heat transfer coefficient and A the effective surface area. The detector and its cooling is a nonlinear feedback system: an increase in the silicon temperature leads to an increased power dissipation in the silicon, which in turn causes an increase in the silicon temperature and so on. This crucial process that has to be avoided is called thermal runaway and it imposes the strongest requirements on the detector module design and on the cooling system because it is crucial to avoid this process.

The sensor technologies under consideration for the ATLAS IBL Project are Planer, 3D and Diamond sensors.

Planar sensors

The planar technology for Pixel is very well known and used with success in many HEP experiments. The drawback is a higher sensitivity to the radiation damage that in the case of the IBL will require operation voltage $\sim 1000\,V$ with higher risk of the thermal runaway. The temperature requirement for the sensor are set to $< -15\,^\circ C$, which in turn means a refrigerants at $-30\,^\circ C$ to guarantee long term operation [15] and sufficient protection against the thermal runaway.

3D pixel sensors

3D Pixels are more radiation hard than Planar, therefore having less cooling constraints. Furthermore the depletion voltage is a factor around 4 lower and the collection time is faster. This is due to its unique design as is depicted in Figure 2.1.
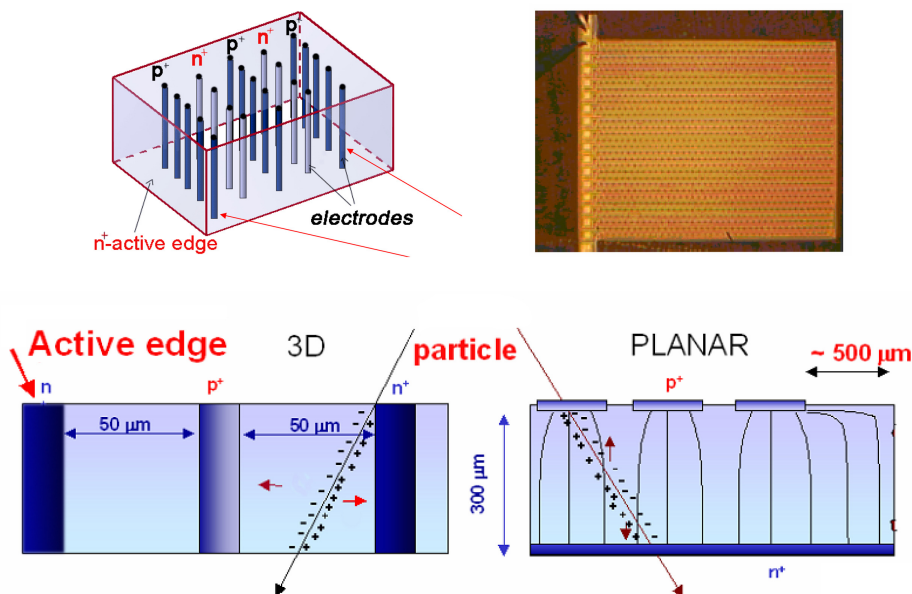

Figure 2.1: 3D silicon sensor has a much smaller distance between its n and p doped parts resulting in desirable characteristics (courtesy of [16]).

The differences are due to the distances between the n and p doped parts which

is sensationally smaller (300 μm to 50 μm). To achieve the same electric field a lower voltage can be applied, the ionized charges have to travel less resulting in faster read-out time and furthermore decreases the change that the charges interfere with damage lattices inside the silicon increasing radiation hardness [16]. For the cooling of these sensors especially the lower depletion voltage is interesting. Although the most power is dissipated in the read-out chips of the sensors, and therefore is the same in planar, 3D and diamond sensors, after years of operation the increase in depletion voltage cannot be neglected, a reduction is therefore a large step.

The limitation of 3D pixels is the production yield and the capacity to produce them in sufficient amount for HEP experiments.

Diamond

Diamond sensors become more popular due to the extreme radiation hardness and leakage currents less than $10 \, nA/cm^2$. The power consumption of the sensors themselves is small reducing in the cooling and support structure [7].

Because the planar sensors are an available technology and present the most challenging requirements for the cooling, the thermal design of the IBL is done to meet their goals, nominally keep locally sensors at $-15\,°C$ with a refrigerant at $-30\,°C$.

2.1.2 Thermal Impedance

A further limitation on the heat transfer efficiency from the sensor to the coolant in the tube is the thermal properties of the structural material of the local support. It must be made of materials with low density to reduce multiple scattering; high thermal conductivity to reduce the temperature gradient and low coefficient of thermal expansion to provide mechanical stability stress release. Carbon based material like TPG have been largely adopted in the present ATLAS Pixel. Carbon Foams are new materials which show even better properties and for that reason are the material of choice for the IBL local support.

The thermal impedance is a measure of thermal efficiency of the local support and can be defined as the ratio of the temperature gradient and the heat density applied. It depends only on the material properties and in analogy with electricity is a measure of the thermal resistance of the passage of heat trough the stack of materials.

$$R = \frac{\Delta T_{s,w}}{q} \tag{2.4}$$

In Equation 2.4 [17], R is the thermal impedance $[°Km^2/W]$, ΔT is the temperature difference between the sensor and the wall surrounding the cooling fluid and q is the power density $[W/m^2]$.

The glue layers between the sensor, the foam and the cooling tube are the locations where the temperature drop is less in control, because of the low thermal conductivity of the glue itself and the intrinsically uneven process of glue distribution at the interface.

2.1.3   Upgrade design

Specific local support design are under development for the upgrade phase I and phase II respectively.

Phase I IBL stave

A cross-section of the IBL stave is depicted inFigure 2.2. The stave will be 840 millimeters long and 18 mm width. The sensors are glued on carbon foam that is stiffened by a carbon fiber sheet with an *Omega* shape [**?**].
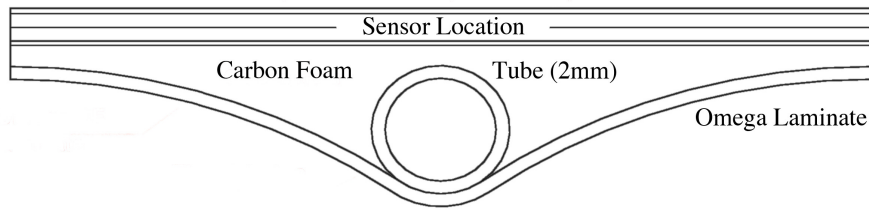
Figure 2.2: Front view of IBL prototype stave, with on top the sensors, supported by carbon foam and the coolant tube which is sandwiched between the *Omega* laminate and the carbon foam.

The cooling tube embedded in the Carbon foam will be in titanium because of its low density and low coefficient of thermal expansion. The inner diameter will be in the range 1.5 and $2\ mm$ with a wall thickness of $\sim 0.1\ mm$. The nominal power that at has to be transferred to the coolant is $76\ W$ or $0.6\ W/cm^2$, and applying a safety factor of 1.5 become $\sim 120\ W$, or $1.0\ W/cm^2$. For an inner diameter of $2\ mm$, the heat flux on the tube will be $22.7\ kW/m^2$.

Phase II sLHC

The local support stave for sLHC Outer Pixel has a mechanical design similar to the IBL with a sandwich of carbon foam between carbon fiber sheets, but the detectors will be mounted on both faces. The total length will be $\sim 1500\ mm$ and the width $\sim 4\ cm$ [17]. The nominal power dissipation will be also more important than the IBl and is estimated at $200\ W$, or $300\ W$ with a safety factor of 1.5. The heat flux seen by the tube will be $31.8\ kW/m^2$.

2.2   Heat Transfer Convection

A fluid can exist out of different forms; liquid and vapor. If a fluid consist purely out one of then the fluid behaves like a mono-phase flow, there are however situations when a fluid consists of both its forms, this is called two-phase flow. Both phases have there own characteristics that are described in the following sections. First, however, the heat transfer coefficient inside cylindrical tubes is defined.

Heat transfer by forced convection of fluids in tubes is a very efficient way to remove heat by electronic equipments and finally particle detectors. The heat transfer coefficient, h, is the main parameter describing the process and, in analogy

with the definition of the thermal conductivity in the Fourier equation, is defined as the amount of heat transferred by conduction trough the laminar stream lines in the boundary layer at the tube-fluid interface.

$$Q = h \cdot (\pi D_i l \Delta T_{w,f}) \tag{2.5}$$

Here Q de applied power $[W]$, h is the heat transfer coefficient $[W/m^2 \, ^\circ K]$, D_i the inner diameter $[m]$ of the tube, l the length $[m]$ of the tube and ΔT the temperature difference $[^\circ K]$ between the tube's inside wall and the coolant.

Forced convection can happen in mono-phase (gas or liquid) or two-phase (liquid and gas) regime with a large variation of the heat transfer coefficient. In the gas mono-phase regime h is lower than in the liquid mono-phase, because of the lower thermal conductivity. Once the heat is transferred to the fluid, the temperature increases accordingly to so called heat capacity and the mass flow:

$$\Delta T = \frac{Q}{C_p \dot{m}} \tag{2.6}$$

Here ΔT is the total temperature increase $[^\circ C]$, Q the applied power $[W]$, C_p is the heat capacity $[J/kg \, ^\circ K]$, and $\dot{m}$ is the mass flow $[g/s]$.

In the two-phase regime (boiling or condensation) the inherent change of phase of fluid (nucleation) allow to exchange a larger amount of heat with heat transfer coefficients a order of magnitude larger than in the case of mono-phase. In two-phase flow the fluid temperature stays constant.

2.2.1 Mono-phase Flow

Liquid mono-phase fluids can be excellent coolants, one example is water, which in liquid form has a high heat transfer coefficient and can be used in a large temperature scale.

Several theoretical models exist for the heat transfer coefficient in monophase regime, based on the Nusselt nubers as is presented in Equation 2.7 [17].

$$h = \frac{Nu_D k}{D_i} \tag{2.7}$$

Here Nu_D is the dimensionless Nusselt number, which provides a measure of the heat transfer convection occurring at the surface between fluid and wall, given by the Dittus-Boelter equation for cooling in Equation 2.8 or by the Gnielinski equation as shown in Equation 2.9 [17].

$$Nu_D = \frac{0.23 Re_D^{0.8} Pr^{0.3} k}{D_i} \tag{2.8}$$

$$Nu_D = \frac{(f/8)(Re_D - 1000)Pr^{0.3}}{1 + 12.7(f/8)^{1/2}(Pr^{2/3} - 1)} \tag{2.9}$$

Here Re_D is the Reynolds number presented in Equation 2.11, Pr the Prandtl number presented in Equation 2.12 and f is the friction factor as shown in Equation 2.13—if the Gnielinski equation is valid—; the latter can also be obtained from the Moody diagram [17]. Equation 2.8 and Equation 2.9 are valid in the following conditions:

$$\begin{bmatrix} 0.7 < Pr < 16,700 \\ Re_D > 10,000 \\ \frac{l}{D} > 10 \end{bmatrix} \tag{2.10}$$

Although in textbooks [17, 18] also the transition region is given, e.g. the Reynolds number is valid if $Re_D > 2300$, caution should be exercised when applying this correlation to turbulent flow, because it can easily result in wrong approximations.

$$Re = \frac{4\dot{m}}{\pi \mu D_i} \tag{2.11}$$

The Reynolds number represents a criterion to distinguish between laminar and turbulent flow, here $\dot{m}$ is the mass flow $[g/s]$ and μ the dynamic viscosity $[Pa \cdot s]$.

$$Pr = \frac{C_P \mu}{k} \tag{2.12}$$

The Prandtl number approximated the ratio of kinematic viscosity and thermal diffusivity inside a tube, thereby giving information how heat is transported perpendicular to the mass flow of the fluid. Here C_p is the heat capacity $[J/kg \,^\circ K]$.

$$f = (0.790 \ln Re_D - 1.64)^{-2} \tag{2.13}$$

The friction factor relates the roughness of the tube inner wall to fluids, which is one of the major causes of pressure drops along tubes [18].

Pressure drop

The pressure drop for mono-phase flow can be calculated with Equation 2.14 [14]. Beside calculating the theoretical pressure drop over a tube, this formula, which is shown in Equation 2.15, can also be used to calculated the mass flow if a good indication for the Reynolds number exists and the pressure drop is known [14].

$$\Delta P = \Omega \cdot l \cdot f^2 \text{ with } \Omega = \begin{cases} \frac{0.31}{Rey^{0.25}} \frac{8\rho}{\pi^2 D_i^5} & \text{if } Rey > 2300 \\ \frac{100}{Rey} \frac{8\rho}{\pi^2 D_i^5} & \text{otherwise} \end{cases} \tag{2.14}$$

$$\dot{m} = \begin{cases} \left(\frac{\pi^2 \rho D_i^5 \Delta P}{0.31 \cdot 8 \cdot l} \left(\frac{4}{\pi \mu D_i} \right)^{\frac{1}{4}} \right)^{\frac{4}{7}} & \text{if } Rey > 2300 \\ \sqrt{\left(\frac{\pi D_i^4 \Delta P}{200 \cdot \rho \mu} \right)} & \text{otherwise} \end{cases} \tag{2.15}$$

ΔP is the pressure drop $[Pa]$ over a certain length, $l\,[m]$ of cylindrical tube with inner diameter $D_i\,[m]$, f is the volume flow $[m^3/s]$ ($f = \dot{m}/\rho$), ρ the density of the fluid $[kg/m^3]$, μ the dynamic viscosity of the fluid $[Pa \cdot s]$,and Rey the Reynolds number as in Equation 2.11.

2.2.2 Two-phase Flow

Two-phase flow is of particular interest for cooling applications, because it provides the highest heat transfer coefficient. It is, however, also the most difficult

situation to describe and there is a lack in literature of reliable theoretical models. Also the models are tuned for specific fluid and specific temperature range. Databases are available in literature for the heat transfer coefficient of many fluids of interest like Ammonia, R134a, R402A, R404A, R502, R123 and Carbon Dioxide. [19, 20, 21, 22, 12, 13]. In the specific case of CO_2 there is a lack of data at low temperatures and small diameter tubes.

Boiling processes

The boiling process happen in several steps which transform liquid in vapor. Assuming a tube where the fluid is entering in liquid formvapor quality is zeroforced convection is dominant, Figure 2.3. Secondly, when the vapor quality increases, small bubbles will nucleate, grow and depart from the heated surface carrying more heat away, this is called nucleate boiling, Figure 2.4. Subsequently, when even more heat is applied the bubbles will become larger, and a transition region arises, after which a stable layer of vapor will form around the wall, this so called dry-out reduces the heat transfer [23].
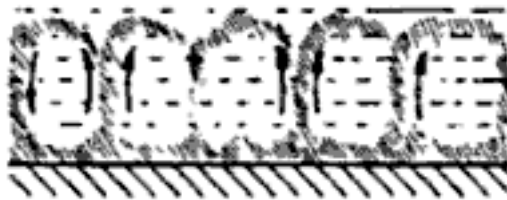
Figure 2.3: Heat from the bottom is exchanged with a fluid by means of natural convection. (Courtesy of [23])
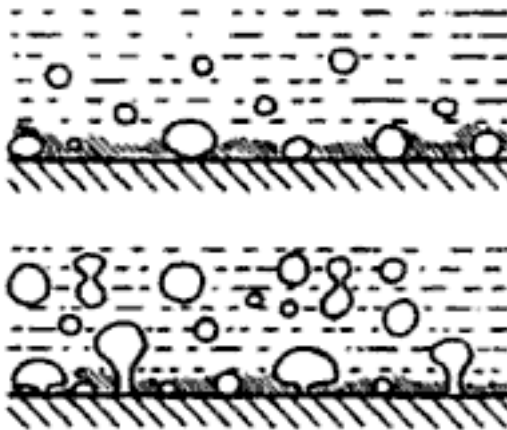
Figure 2.4: Heat from the bottom is exchanged with a fluid by means of nucleate boiling. In the upper picture a low heat flux is applied while at the bottom picture a higher heat flux is applied. (Courtesy of [23])

The behavior of the fluid under evaporation in tubes is visualized in Figure 2.5. Interesting flow regions for refrigeration are; intermittent flow (which is the col-

lection of bubble to slug flow), and annular flow. The dry-out/mist flow, which is the part where the tube wall is covered by vapor instead of liquid is less interesting for refrigeration because the heat transfer reduces, but it is therefore of out most importance to now when it will happen.
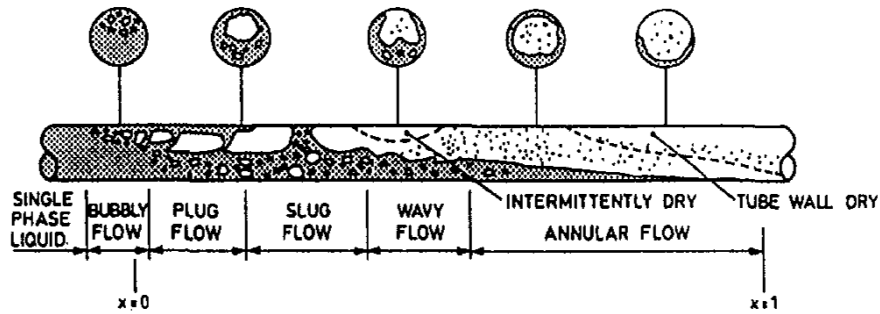
Figure 2.5: Boiling pattern of two-phase flow inside horizontal circular tube. As soon as the wall is not completely covered with liquid the heat transfer coefficients reduces.

At the same vapor quality it is possible to have different kind of flow, because also the coolant's mass flux has influence. This can be depicted in a flow pattern map as is done in Figure 2.6, which are flow pattern maps of R-22 under different heat loads.
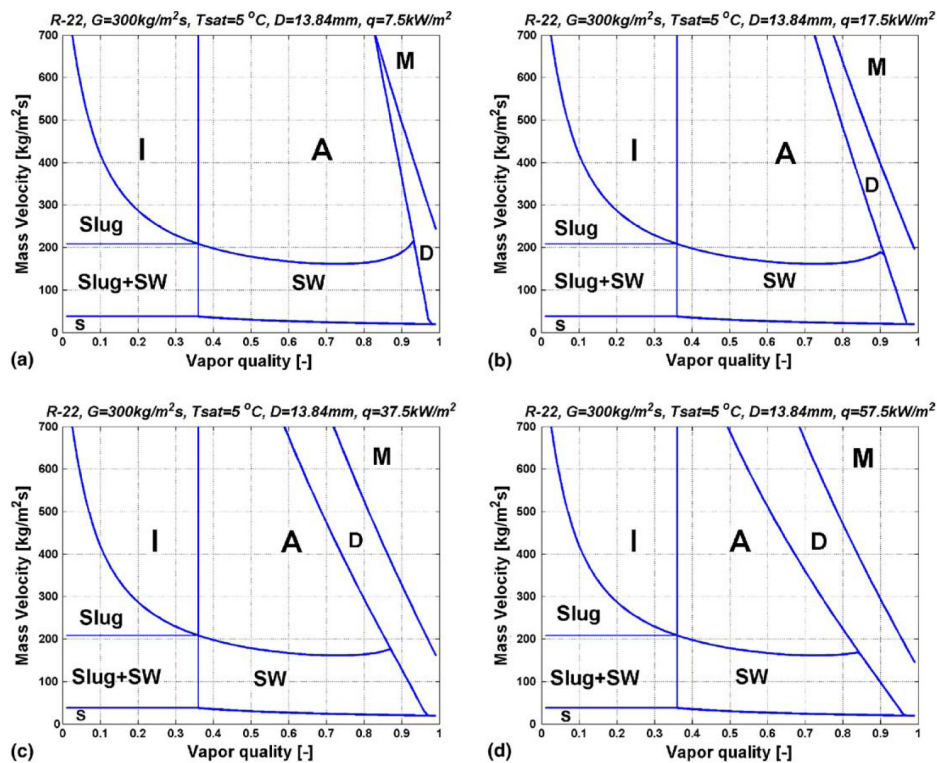
Figure 2.6: Flow pattern maps of R-22 for $D_i = 13.84\ mm$, $G = 300\ Kg/m^2s$ and different heat loads. I stands for intermittent, A for Annular, D for Dry-out, M for mist and SW for stratified wavy. (Coutesy of [24]).

Intermittent flow

Intermittent ow is the region at low vapor quality and represents the part where forced convective boiling is mostly dominant. The tube wall is fully surrounded by liquid and the heat transfer is large.

Annular flow

Annular ow is represented by ow that is in contact with the heated surface. Due to the forced ow, nucleating bubbles that arise will be transported away quickly resulting in an increasing heat transfer when the bubbles become larger, as long as there is contact between the wall and liquid.

Dry-out

In the dry-out regime there is no direct contact between the heated surface and the liquid inside the tube, instead it is in contact with vapor which has a much lower heat transfer. Depending on the coolant characteristics, this results in a sharp decline in heat transfer.

Mist flow

When the liquid bubbles in the dry-out flow decline mist flow arises. This flow contains mostly gas and therefore has a low but stable heat transfer.

2.2.3 Boiling characteristics CO_2

The high operating characteristics of CO_2 results in high vapor densities, very low surface tensions, high vapor viscosities and low liquid viscosities. The low surface tensions in combination with the high pressures have major effects on nucleate boiling heat transfer characteristics. Clear dominance of the nucleate boiling over forced convective boiling result in much higher heat transfer coefficients. Furthermore it has been shown that significant deviations between general and CO_2 flow pattern maps exist: dry-out in evaporative CO_2 occurs at moderate vapor quality and heat transfer is declining rapidly, or even steep. Specific CO_2 models have been under development, but are to extended to summarize here. They try to describe two-phase CO_2 completely, including predictions of heat transfer coefficient, flow pattern maps, pressure drop models [12, 13].

Chapter 3

Experimental setup

3.1 CO$_2$ Blown system

A versatile, scalable and cheap cooling test stand, called Blown System, has been developed at SLAC to characterize the heat transfer properties of CO$_2$. Liquid CO$_2$ is spilled out from a CO$_2$ bottle to the experimental setup where it passes through a ow meter that measures the ow rate and temperature of the fluid. Subsequently, the fluid flows through an absolute pressure sensor and the first heat exchanger. Here an external chiller cools the CO$_2$ down to $10\,^\circ C$ using water, and $-10\,^\circ C$ if a water glycol mixture is used. Then the fluid passes through a second heat exchanger where cold CO$_2$ flows in counterflow, thereby bringing down the temperature of the CO$_2$ even more. After this pre-cooling area, the fluid passes a needle valve: here the pressure is decreased, and consequently the temperature drops. Subsequently, the CO$_2$, which is now at the desired temperature, will enter the test area where it first flows through a gauge pressure sensors and then enters the test tube. A second gauge pressure sensor is placed at the end of the tube, thus allowing the measureming of the pressure drop over the test tube.
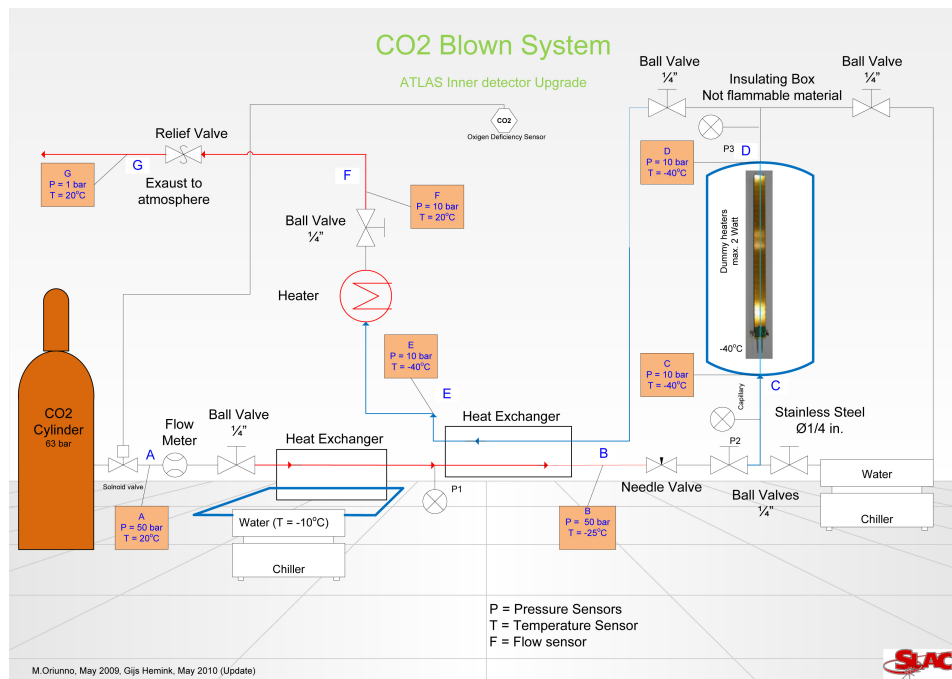
Figure 3.1: Improved CO_2 blown system, with an additional heat exchanger and a decouple system to switch to water measurements.

Before the fluid is heated up to room temperature and blown in open air, it rst ows through the (second) heat exchanger: the still cold uid is used to bring down the temperature of the entering CO_2. A pressure regulator valve is placed after the heater to control the pressure (hence, the coolants temperature that enters the test area). The implementation of two ball valves before and two after the test area allows for a smooth switch between the usage of CO_2 or water as refrigerant. The blown system can be disconnected from the test area and the connected (water) chiller can then be used. At the end of the system a relief valve (opens at 40 bar) is placed in case pressure inside the system builds up to high. Finally, a Oxygen Deciency Sensor is placed above the setup: in case of low oxygen it shuts down the outside placed bottle by means of a solenoid valve.

Further details about the used hardware and sensors is summarized in subsection 3.3.1.

3.2   Improvements made to CO_2 Blown system

The knowledge of the blown systems functioning as described in **??** was at this thesis's start inadequate. One of major changeless before measurements could be done was to fully understand the system and to improve the deficiencies. In this paragraph the main issues and applied or proposed solutions are shortly explained.

3.2.1 Mass flow regulator

The first main issues concerned the mass flow rate, or mass flux. The mass flow is regulated by the needle valve that also is responsible for a pressure drop after the pre-cooling of the entering CO_2. This causes the transition from vapor flow to the desired two-fase flow. Unfortunately it gives an inconstant flow rate as depicted in Figure 3.2.
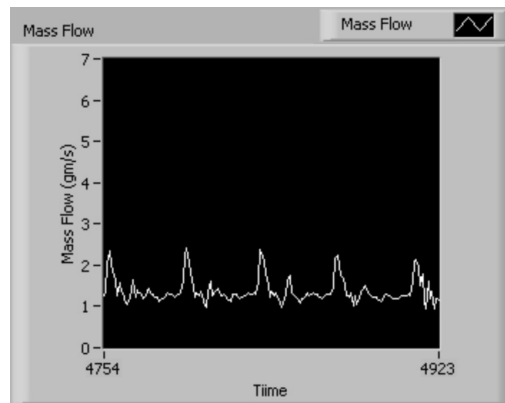
Figure 3.2: Measurement of the mass flow, although it should give a constant rate, deviations of more then 100% are visible.

Consequently the mass flux increases and the pressure rises, thereby increasing the saturation temperature. The result is a vicious cycle, and a necessary equilibrium is not reached, making it impossible to do repeatable measurements.

This problem arise because the needle valve is used at its lower limit creating already a unstable situation. However, it works fine in some cases. Two additional reason have been found: a pressure wave inside the system, and the rapid pressure decline of the CO_2 bottle. An old pressure sensor was found to be attached to the system, connected after the needle valve, but before the test area: removing this piece solved the first problem. The solution to the second problem is to change the bottle, if running at flow rates of $1\ g/s$ is a necessity. An other option is to increase the flow rate to above $2\ g/s$. The updates made resulted in a stable mass flow.

3.2.2 Temperature sensors

The used temperature sensors should have a deviation of $\pm0.2\ °C$ at most, however deviations up to $\pm1.0\ °C$ have been measured between sensors. This can be explained by the thermal impedance of the tube and used glue. This is solved by using a different glue technique as is shown in Figure 3.3. Moreover, calculations show that the sensors wires also have to be connected to the tube, otherwise they will transport the ambient temperature to the sensors, thereby influencing the measurement (this calculation is done in detail in **??**).
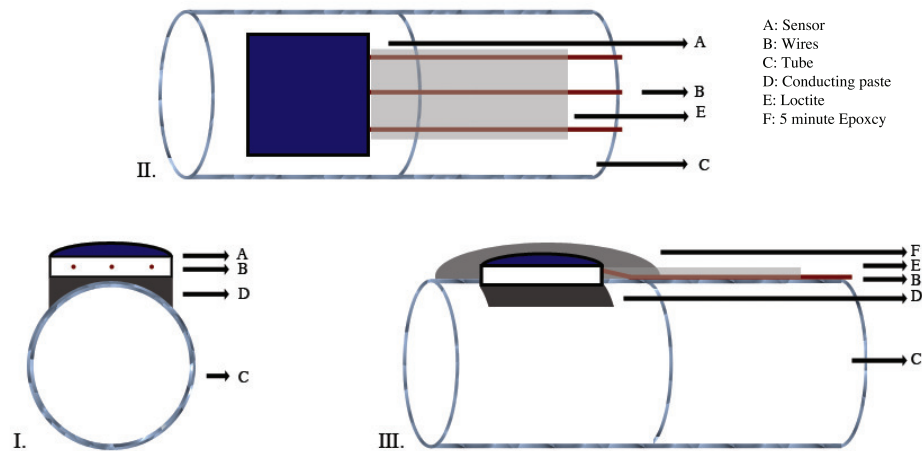
Figure 3.3: The three steps in the glueing process. First the sensor is firmly attached with conducting paste to the tube. Subsequently the wires are glued as firmly as possible to the tube with Loctite. The final step is to cover the sensor with epoxy to make sure no heat from around the tube comes in contact with the sensors, furthermore it also protects the sensor to slip off in case of shocks.

However, this gluing process does not solve the large deviations that have been found with the two sensors implemented inside the pressure sensors: they are not glued to anything, but are in direct contact with the cooling fluid. It is possible that the temperature gradients during the start up of the CO_2 blown system damages these sensors. They are essential for the calculation of the heat transfer coefficient – the slope of the fluid is calculated from these two values – therefore, a calibration has to be done. For water measurements the chiller's temperature can be used as a reference, but this is not possible for CO_2. Here the properties of the two-phase flow can be exploited, because the temperature equals a certain pressure. Hence, if the pressure is know at the inlet of the tube – which is, with a smaller error relative to the temperature sensors – the corresponding temperature is know.

3.2.3   Second heat exchanger

Due to safety reasons the CO_2 bottles are located outside the building. The implications are that the sun is shinning on the bottle for a good part of the day, thereby heating up the bottle and consequently increasing the flow temperature and pressure. This effect has significant influence on the measurements, making it hard to reproduce stable circumstances.

The solution was to make a second heat exchanger that pre-cools the CO_2 from the bottle to a temperature independent of the sunshine. This is achieved by putting the chiller, which is not used for CO_2 measurements, on this heat exchanger. The temperature can be set as low as $10\ ^\circ C$ if the cooling fluid is water, and even lower ($-10\ ^\circ C$) if a water (50%) glycol (50%) mixture is used.
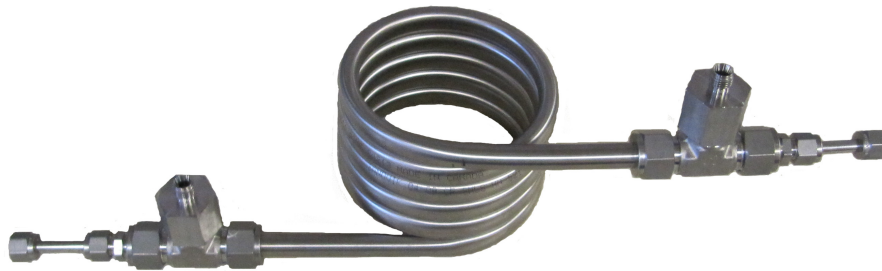
Figure 3.4: Second heat exchanger that is placed after the mass flow meter but before the original heat exchanger.

The heat exchanger is shown in Figure 3.4 and is directly placed after the mass flow meter in Figure 3.1. The improvement not only makes the system independent of the sun shinning on the bottle, in combination with the original heat exchanger it also lowers the vapor quality. For $-30\ °C$ the vapor quality is now almost zero, which makes it possible to do a more thorough study of the tubes.

3.2.4 Water versus CO_2 measurements

When a new tube has to be analyzed, first a water measurement is done. However, letting water into the system results in problems when the switch to CO_2 is made. Getting the water out of the blown system, especially out of the mass flow meter and the needle valve, results in freezing phenomena when CO_2 is switch on if this is not done properly. A needle valve blocked with ice crystals interrupts the flow of CO_2 ruining the measurement. Furthermore, CO_2 reacts with water to form H_2CO_3 (Carbonic acid), which can deposit itself onto the wall of the test tube influencing all the measurements.

A solid solution to this problem has been made by implementing two ball valves before the inlet pressure sensor and two ball valves after the outlet pressure sensor: it is now possible to switch between two different fluids. A much smaller part now has to be flushed with N_2 gas to lower the humidity, decreasing the change of ice inside the blown systems critical parts, without modifying the system.

3.2.5 Electronics

The used electronic read-out system was confusing. Wires from the Labview blocks had to be connected to the right sensor two meters further. Furthermore, the distribution of power to the pressure sensors was not clear, cables could not be changed when broken and the distance of the test area to the blown system was limited. Because National Instruments equipment makes it difficult to disconnect sensors, a plug and play system for the temperature sensors has been design, consisting of a box with 27 connections. This box is always connected to the National Instruments blocks (NI 9217), however the sensors can be disconnected quickly. For the other used sensors a connector has been placed directly on the National Instrument block (NI 9205) making them also changeable. The distribution of power

has been changed to a boxed version, the same applies for the common ground: these boxes are depicted in Figure 3.5 and Figure 3.6.
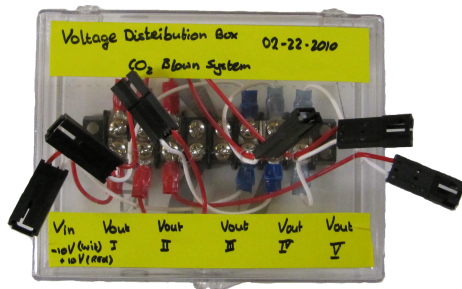
Figure 3.5: In this picture the voltage distribution box is shown: it has five output connectors.
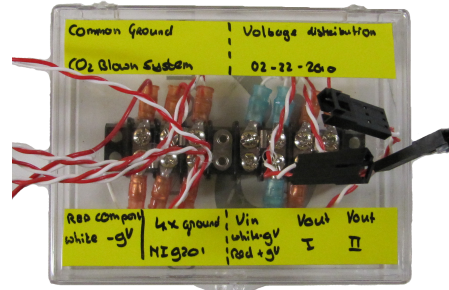
Figure 3.6: In this picture the voltage and ground box is shown: it has three grounds and two output connectors.

The system is now transformed to a plug and play system where sensors can easily be connected, broken cables can be taken out fast and changed by new ones, the distance between the test area can be made as long as needed, and most of all, it is now clear where and how each sensor has to be connected.

3.2.6   Power safety box

A stronger power supply was needed due to the decrease of overall resistance in different tubes wall sizes. In operating mode it was found out that the power supplies safety system had shortcomings. Therefore an hardware based safety system has been design that consists of two independent switched placed in series, they are temperature triggered (Figure 3.8) and are mounted inside a box placed between the wall and power supply. The electrical scheme is depicted in Figure 3.7.

The figure contains a circuit schematic with the following labels:

```
PS1
IN: 110V 20A AC
OUT: 20V 20A DC

BOX

GREEN          White      BLACK

T2          COPPER

GREEN

T1      COPPER    TH1    White    TH2        GREEN
                  SW2             SW3
                  SW2    BLACK    SW3
                                           GREEN

BLUE                          SW1
min 16 AWG    BLACK
     F1
     6.0 AMP                F

          BROWN
          min 16 AWG
                           GREEN
     min 16 AWG
```

```
F1        Fuse holder
F1        Fuse 6A
T1        Temperature sensors (trigger)
T2        Temperature sensors (trigger)
TH1&TH2 Therm Coil Manufacturing CO.
TH1&TH2 TD1 2574K
PS1       AGILENT 6032A
SW1       Switch (ON/OFF)
SW2       Thermostat switch
SW3       Thermostat switch

Comment:

TH1 and TH2 are mechanically switched
they do not need power to operate but
work as a thermostat.
The wires from T1&2 to TH1&2 are copper
and have a fluid inside which controls
the switches.
The start mode (if given a reference
temperature) is ON.
```

```
SLAC
ATLAS IBL COOLING CO2 SAFETY BOX
SD 256-100-41 - C00
G Hemink    Rev 1.0        page 1 of 1
            5/19/2010
```

Figure 3.7: Electric scheme of the power supply safety box, consisting of two switched placed in series. The temperature sensors, T1 and T2, are placed inside the isolation box of the tubes and are then set to a reference value. If this value is reached at one of the sensors it breaks the circuit and the power supply is shut down. Also a fuse and on/off switch are implemented conform SLAC safety rules.

Figure 3.8: Temperature sensor from the power safety box attached to the tube, an electrical isolation layer is placed in between to prevent a short circuit.

The box has been approved by the SLAC EEIP department and prevents the prototype from overheating.

Power connections

The connection of the wires from the power supply to the tube have also been improved. This is visualized in Figure E.1 where to copper blocks are cramped over

the tube allowing fast changeability to other tubes and without creating additional resistance in the system. They have been made for all the test tubes diameters.

3.2.7   Thermal isolating box

There was no appropriate isolation box available, therefore a new one has been designed and build: with a length of 1.70 by 0.15 meter, it is able to contain both test tubes for the phase I and the phase II upgrades. It is filled with non-flammable isolation material and can be closed by two latches. The box is depicted in Figure 3.11.
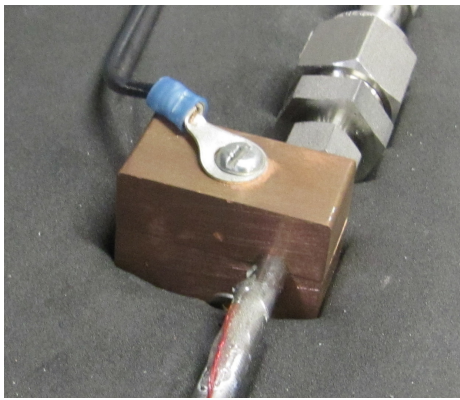
Figure 3.9: Two copper blocks cramped around the tube distributing the current along the tube. They are connected to a power supply.
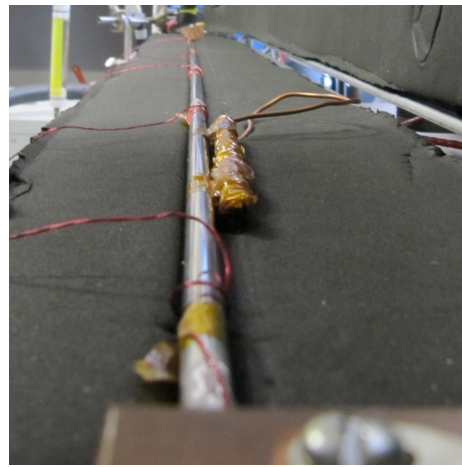
Figure 3.10: Tube placed inside the isolation box. Visible are the temperature sensors wires leaving the box and a safety temperature sensors.
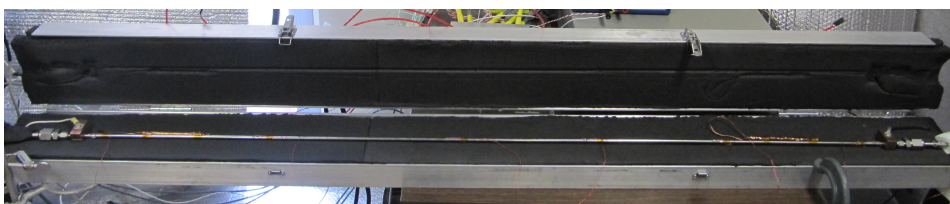
Figure 3.11: New isolation box with a length of 1.70 meter is it capable of running tests for the IBL and sLHC pixel upgrades.

3.3   Data acquisition

The data acquisition of this setup consists of three parts: hardware (subsection 3.3.1), read-out system (subsection 3.3.2), and a data analyzing program (subsection 3.3.3).

3.3.1 Hardware

Various sensors are used to determine the necessary data and supply power, they are summarized in Table 3.1 including model and range.

Sensors	Model	Range
Absolute pressure sensors	PTX 7200	$0 \rightarrow 1400$ bar
Chiller (max. 2.9 kW)	PolyScience 6561T	$-10 \rightarrow 35\,°C$
CO_2 bottle	Airgas	50 lb
Flow meter	Rheonik RHM 015	$0.004 \rightarrow 0.6$ kg/min
Gauge pressure sensors	Druck DPI 104	$0 \rightarrow 690$ bar
Humidity sensors	Apollo HIH series	$0 \rightarrow 100\%$ RH
Labview DAQ	NI c-DAG 9172	9 block places
Labview blocks	NI 9205 & NI9217	1 & 8 blocks, resp.
Power supply (applied heat)	Agilent 6032A	20V, 50A
Power supply (electronics)	BK precision 1786A	$0 \rightarrow 30$V
Safety sensors	Therm Coil TD1 2754K	$60 \rightarrow 250\,°F$
Temperature sensors	OmegaFilm Pt Class A	$-50 \rightarrow 450\,°C$

Table 3.1: Overview of used electronic device and sensors.

The data acquisition of the RTD temperature is done by the specialized Labview block, NI9217. The value of the pressure sensors can be deduced from the current used to operate the sensor. The NI9205 however reads only the voltage drop, therefore a resistor is placed over each pressure sensors. It is then possible to measure the voltage drop, which is translated back to current in Labview. The humidity sensors, the mass flow value and the fluid temperature, which is measured by the mass flow meter, are also read out in this way. In Figure 3.12 the four different electrical schemes are depicted.

(a) A

Red   Red

V1

Pressure   Blue   Black
sensor   R1

Red   Black

NI 9205   V1 = 18V
Port 4 & 5   R1 = 205Ω
Current read-out

(b) B

Rheonix
RHE 07

20 mA +
                              R1   NI 9205
                                        Port 0
Loop2 -   Current Read-Out

Temperature
sensor

20 mA +
                              R1   NI 9205
                                        Port 1
Loop1 -   Current Read-Out

Mass flow
sensor   R1 = 401.5Ω
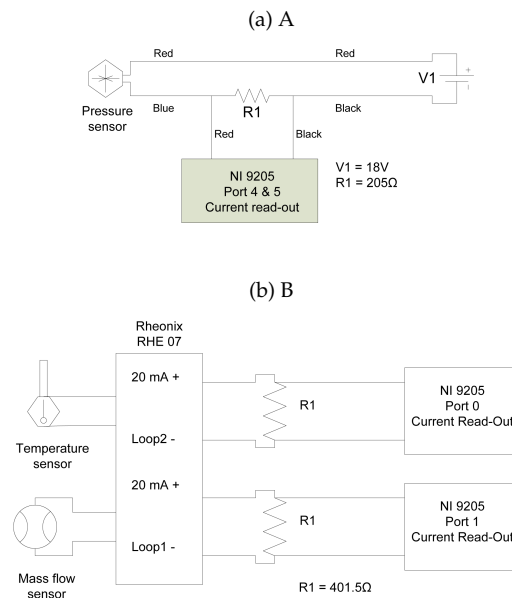
Figure 3.12: Electrical schemes sensors that make it possible to determine the current.

3.3.2 Labview

A Labview read-out program has been developed from the basic program that existed. Upgrades that have been made are the new user lay-out, which besides showing a diagram of the blown system with the appropriate sensors on the right spot, also has five graphs that show the temperature of the sensors attached to the tube, the other temperature sensors, the mass flow and the pressure sensors live. Colors indicate if a temperature sensor is working (green/red), furthermore the system detects and displays if a CO_2 bottle is used (gray in CO_2 bottle turns green), if a fluid is flowing in the system (balk between temperature sensors turns blue) and an indicator glows when a current is applied over the tube. A general overview of the front panel interface is depicted in Figure 3.13.

Figure 3.13: Labview front panel interface with on the upper right the power supply controls, adjacently graphs are placed. At the bottom a schematic view of the blown system including sensors values is visible.
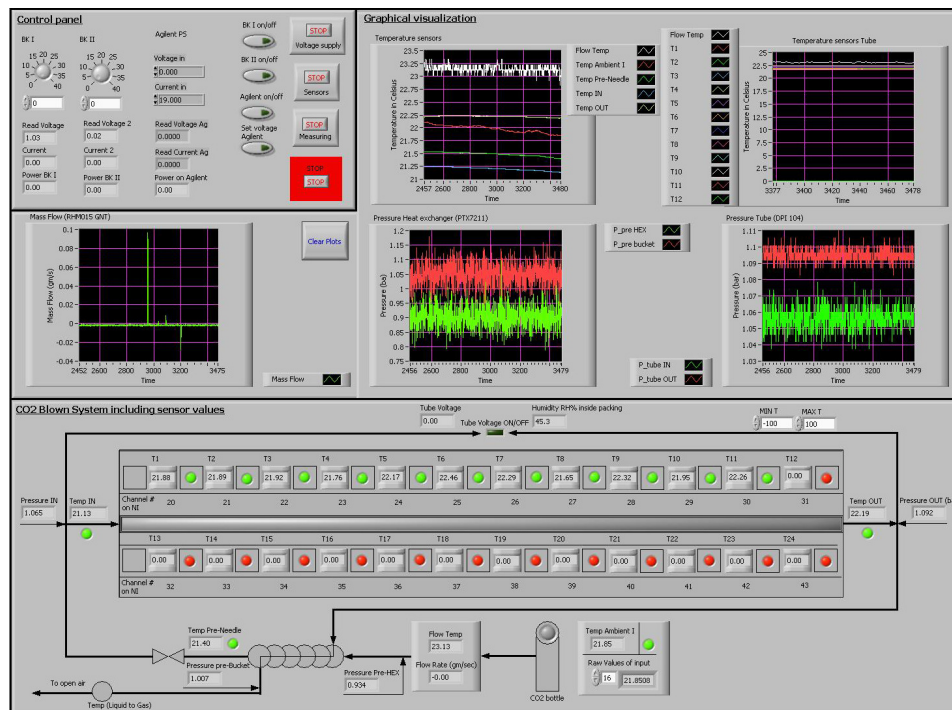
A special controlling program for the Agilent power supply has been written. That besides giving control over the device also included safety software: iff one of the sensors measures a temperature above $80\,^\circ C$ it shuts down, furthermore when the applied power becomes higher then $80W$ an approval has to be given by the user. Finally, a lot of minor improvements have been made, e.g. better structure, more sensors, safety indicators and writing the acquired data to a file.

3.3.3 Matlab

A Matlab program has been written to analyze the data taken by Labview. Using the calculations as presented in section 3.4, the heat transfer coefficient and thermal impedance are calculated for tubes and prototypes stave, respectivitly. Furthermore, the program compares the calculated heat transfer coefficient with the CO_2 prediction models of [12, 13], it compares the pressure drop with the pressure drop models, determines the flow pattern maps and calculates relevant points in the pressure enthalpy diagram, and finally saves all the related graphs to the computer. It is also possible to run a simulation of a certain tube with specific characteristics. A short manual to add a new measurement to the program and to analyze that file can be found in Appendix B.

3.4 Measurements

Four different experiments are proposed to accomplish this thesis goals. The first two concern test tubes with small diameters. The second experiment is to determine the heat transfer coefficient of CO_2 of test tubes, however, before these can commence, first, for every tube the heat transfer coefficient with water as coolant is determined. This is done because the theoretical predictions are accurately known, making it possible to quantify the working of the experiment. When the results are satisfying, measuring the heat transfer coefficient of CO_2 can start. The other two experiments concern IBL prototype staves experiments. The first of these is to determine the thermal impedance of Carbon Foam: water is used as coolant for the same reason it is used in the control measurement for the CO_2 experiment. The last experiment is to determine the heat transfer coefficient of CO_2 using the tube embedded in the prototype stave, this is possible when the thermal impedance has been calculated.

3.4.1 Measuring the heat transfer coefficient of CO_2

Control measurement

Before the heat transfer coefficient of CO_2 is measured, a control measurement for every tube, using water at various temperatures (15, 20 25 °C), takes place. By applying different heat loads the heat transfer coefficient is determined in the same way as will be explained in the description of the CO_2 measurement. Subsequently, this is will be compared with the the theoretical heat transfer coefficient prediction of water to see if it agrees. If so, CO_2 measurements can commence.

CO_2

When **??** is used to calculate the heat transfer coefficient of CO_2, the temperature difference between the coolant and inner tube wall is measured with various heat loads, different coolant temperature and mass fluxes in the tube. Multiple temperature sensors are attached along the test tube to measure the outside wall temperature. Subtracting the value calculated with Equation 3.2 from the measured temperature results in the inner wall temperature. Measuring the pressure at the inlet and the outlet of the test area enables the calculation of the fluids temperature along the tube by linear interpolation between the two measured values. This is possible because evaporating fluids maintain a specific pressure at a given temperature as is shown in Figure 3.14.
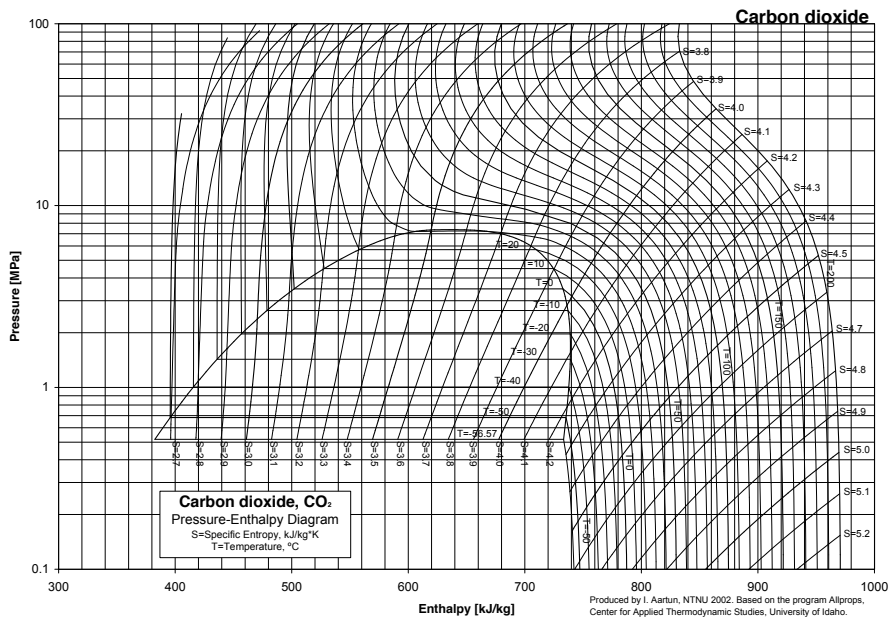
Figure 3.14: Pressure-Enthalpy diagram with correlation between pressure and temperature inside the parabola: fixed pressure equals fixed temperature.

The tubes wall works as a resistor around the coolant creating a temperature difference as is depicted in Figure 3.15.
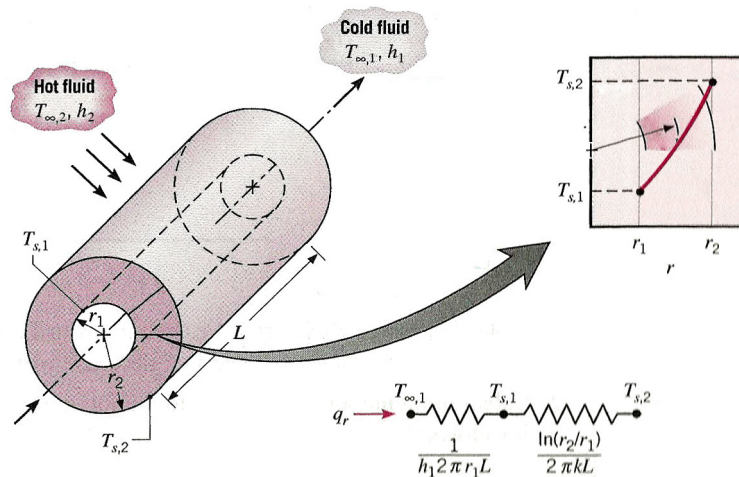
Figure 3.15: Hollow cylinder with convective surface conditions. Here an cold fluid flows through the tube, thereby absorbing heat that is applied on the outside wall of the tube by a warmer fluid. (Courtesy of [17]).

The temperature on the inside of the tube is therefore lower, as can be seen

on the top right. A simple view on this situation is the analogue with an electric circuit as is done on the lower right: here heat represents the transported current; temperature difference, the voltage; and the tube's wall, the resistor.

In experiments a current I is applied on the outside wall of the tube, this wall works as a resistor creating a temperature gradient perpendicular through the tube's wall, as is described in Equation 3.2 were the gradient is calculated [17].

$$\Delta T_w = \frac{Q \ln(r_o/r_i)}{2\pi k l} \tag{3.1}$$

With r_o and r_i the outer and inner radius $[m]$ of the tube, Q the applied power $[W]$ and k the thermal conductivity $[W/m\,^\circ K]$.

The effective power, or heat load Q Equation 3.2, applied over the test tube can be determined by reading out the current and multiple the square product of I with the temperature correct resistance, which can be calculated with Equation 3.3.

$$Q = I^2 \cdot R(T) \tag{3.2}$$

here I is the current $[A]$ and $R(T)$ the temperature dependent resistance $[\Omega]$ as represented in Equation 3.3,

$$R(T) = R_{ref}\left[1 + \alpha \cdot (T - T_{ref})\right] \tag{3.3}$$

which is deduced from the *Bloch-Grüneisen* formula [25] for a resistances R at temperature T with a reference resistance R_{ref} at T_{ref} and α a material constant $[^\circ K^{-1}]$.

3.4.2 Thermal Impedance

The thermal impedance of a prototype stave is determined with Equation 2.4, using water as coolant. The effective power Q can be determined in the same way as done in subsection 3.4.1, but now has to be divided by the surface area ($A = \pi \cdot D_i \cdot l$) to calculate the power density q. The temperature difference between a sensor and the outer tube wall cannot be measured directly. Equation 3.4 approaches this another way using **??**, making it possible to calculate $\Delta T_{s,w}$. and subsequently, the thermal impedance.

$$\Delta T_{s,w} = \Delta T_{s,f} - \Delta T_{w,f} = \Delta T_{s,f} - \frac{Q}{\pi D_i h_{water} l} \tag{3.4}$$

Temperature sensors are placed on top of the prototype pixel sensors to measure their temperature on various places along the stave. The fluid temperature is determine by linear interpolation of the temperature between two temperature sensors that are placed inside the pressure sensors (they are in direct contact with the coolant). From a theoretical point of view also Equation 2.6 can be used, because the coolant temperature at the inlet of the stave is known from the chiller; the pressure sensors cannot be exploited in this case because a mono phased fluid is used. A correction for the wall thickness has to be made, as is done in subsection 3.4.1 using Equation 3.2: this is done to calculate the outer wall temperature from the inner wall temperature otherwise the thermal impedance of the tube is included with the thermal impedance of the Carbon Foam. Finally, h_{water} can be determine as is described in subsection 2.2.1 using the characteristics of water (based on NIST database [26]) at the local fluid temperature.

3.4.3 Measuring the heat transfer coefficient of CO_2 using staves

The heat transfer coefficient of CO_2 inside tubes can also be determined using the prototype stave when the thermal impedance of the foam is know. Rewriting Equation 3.4 using Equation 2.4 results in Equation 3.5, making it possible to subtract interfering variables, thereby reducing the situation as if the sensors where placed on the outer wall of the tube inside the prototype stave.

$$\Delta T_{w,f} = \Delta T_{s,f} - R \cdot q \qquad (3.5)$$

Here $\Delta T_{s,f}$ can be measured experimentally as explained in the previous section. This can than be implemented in the general formula for the cylindrical heat transfer coefficient, see Equation 3.6.

$$h_{CO_2} = \frac{Q}{\pi D_i l \left(T_{s,f} - R \cdot q \right)} \qquad (3.6)$$

Chapter 4

Results

Measurements on the IBL prototype stave have been performed using water as coolant to determine the thermal impedance. Furthermore, the heat transfer coefficient of CO_2 using small diameter tubes and the IBL prototype stave have been measured under various mass flows while variating the coolant's temperature and the applied heat flux. Moreover, the results have been compared to prediction models. In Appendix C an overview of the tubes properties and the taken measurements can be found; the main results are presented in the following paragraphs.

4.1 Thermal impedance IBL pixel prototype stave

The IBL prototype stave has been investigated using water as coolant to determine the thermal impedance of the Carbon Foam. Subsequently, the data has been analyzed and is presented in subsection 4.1.1. The prototype arrived damaged at SLAC National Accelerator Laboratory therefore reparations had to be made. This lead to an interesting discovery, which can be found in subsection 4.1.2.

4.1.1 Thermal Impedance Carbon Foam

The thermal impedance has been measured as described in subsection 3.4.2, by ten temperature sensors attached along the pixel prototype stave. Using water at temperatures of 5, 10, 15, 20 and 25 °C while applying a power around 0, 32, 48, 64, 80 W, the thermal impedance under 20 different experimental conditions has been determined. The result of two single measurements are shown in Figure 4.1 and in Figure 4.2 a graph that combines four measurements is presented.

(a) (b)
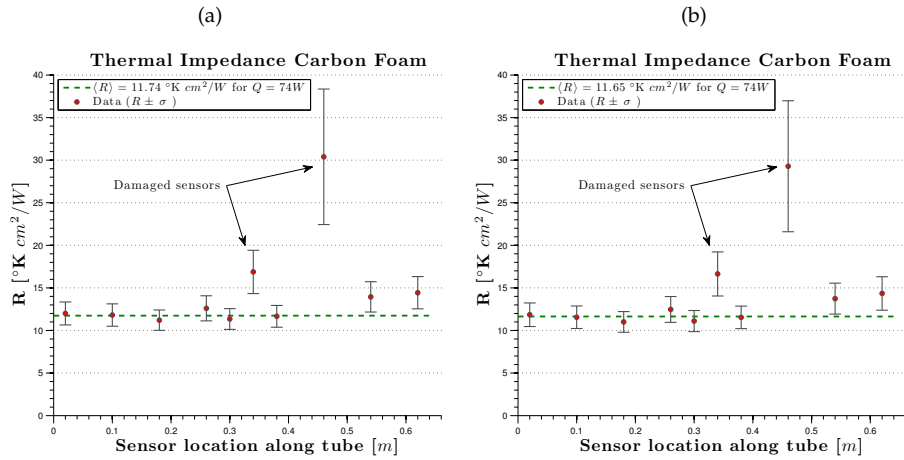
Figure 4.1: Thermal impedance of IBL prototype stave, measured with 10 temperature sensors along the tube at two different temperatures, $T = 10\,^{\circ}C$ (4.1a), $20\,^{\circ}C$ (4.1a), both with an power dissipation of $74\,W$. The green line indicates the average value based on sensors 1 to 5 and sensor 7. The other sensors are found to be damaged or influenced by the damaged sensor. The data points with corresponding errors are plotted with red and black, respectivity.

Figure 4.2: Measurement of the thermal impedance of the Carbon Foam used in the IBL pixel prototype stave. The four measurement have been taken at $74W$. The average calculated value, $R = 11.62\,^{\circ}Kcm^2/W$, is represented by the green line. In this calculation the damaged sensors are not taken into account.

The thermal impedance measured at the positions of the damaged sensors is not taken into account because at those location an additional thermal resistors exist thereby increasing the local thermal impedance but without changing the material properties of the Carbon Foam.

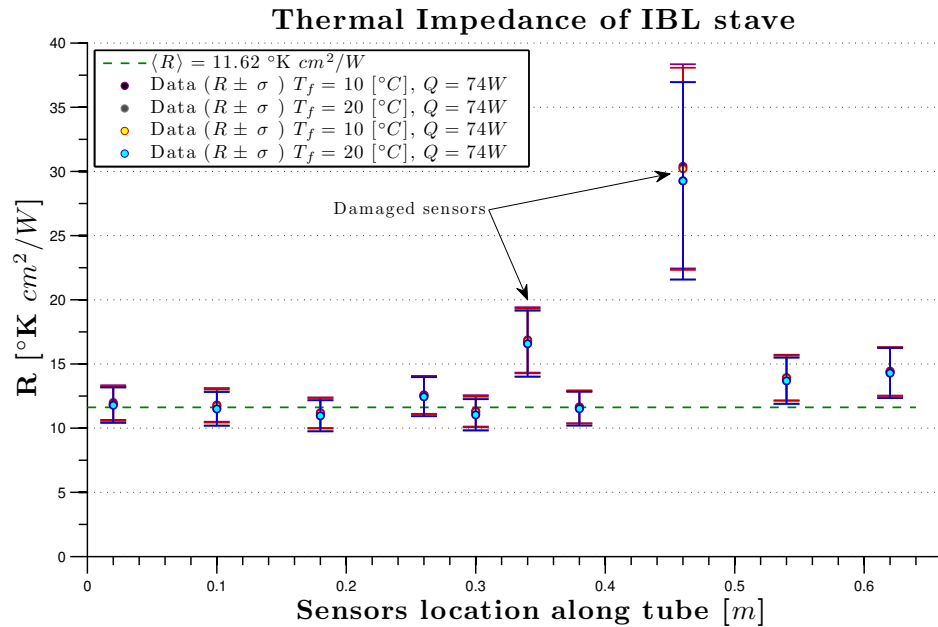The calculated average value is $R = 11.62\,°Kcm^2/W$. The theoretical value calculated with finite element analysis at various institutes is $R = 5\,°Kcm^2/W$. In the next section it is made clear that the quality of the foam is not as would have been expected. This could be one of the reason why the measured value is a factor 2 higher, furthermore it is know that difficult glueing processes that attach the foam to the sensors have a large influence on the thermal conductivity.

4.1.2 Quality of the foam

The reparation that had to take place to repair the damaged stave revealed the inner structure of the Carbon Foam around the tube. Two photographs (see Figure 4.3) that were taken while the stave was under repair show a large hole below the tube. The contact between foam and tube is there reduced, thus increasing the thermal impedance.

(a) Front view of Carbon Foam with 2 mm tube coming out.
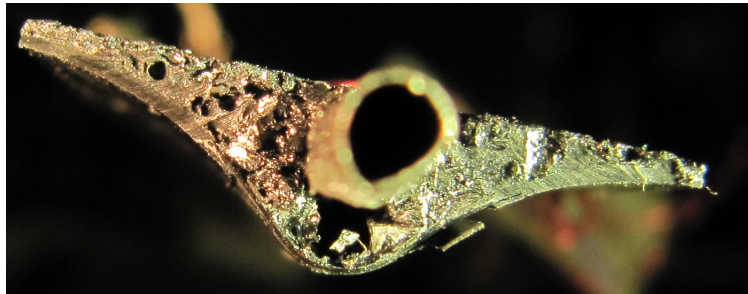
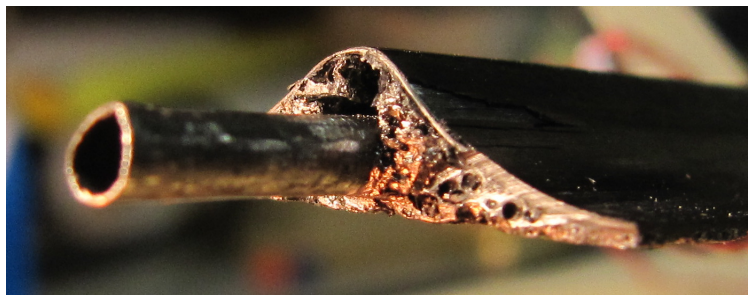(b) Front view at an angle of 45 ° on the damaged area (stave is placed upside down).

Figure 4.3: Cross-section of the IBL prototype stave, while it was under repair.

Dummy sensors

Besides the bad contact between tube and foam also two heaters were found slightly de-attached. The thermal impedance on those places is therefore higher

because additional thermal resistors, for example air, influence the measurements. The material property of the foam is thereby not changed, therefore the damaged sensors are not taken into account in the previous section.

4.2 Heat transfer coefficient

The heat transfer coefficient of CO_2 has been determined for four different tubes, all with a length around $1500\ mm$. Before this measurements could commence, first the heat transfer coefficient of water has been measured using these tubes to see if the theoretical prediction for the heat transfer coefficient of water could be reproduced. This was also a check to see if the data acquisition system worked accurately. These results are presented first, then the results concerning CO_2 and the ATLAS phased upgrades are shown.

4.2.1 Introduction

Four different tubes are used to measure the heat transfer coefficient of both fluids. Three are made of stainless steel (SS) but differ in inner diameter and wall thickness. 6 sensors are attached along each tube to measure the outer wall temperature when a heat flux is applied. The fourth tube is made out of Titanium (Ti): this is the material used in the prototype staves. It has 10 temperature sensors connected along the tube. In the next section the tubes are called SS RW-12, SS RW-14, SS Swagelok an Ti RW-14, and have an inner diameter of $D_i = 2.16\ mm$, $D_i = 1.6\ mm$, $D_i = 4.57\ mm$ and $D_i = 1.6\ mm$, respectively. More characteristics of the tubes can be found in Appendix C.

4.2.2 Water

The heat transfer coefficient of water has been determined used water at different temperatures while applying different heat fluxes on the tubes. For each fluid temperature (15, 20, 25 $°C$) an effective power between 0 and $300\ W$ has been applied. The mass flow has been kept constants per tube because this was regulated by the used chiller, and thus dependent on the tubes diameter. The results of the four tubes are presented below.

In Figure 4.4 the results for the SS RW-12 tube are presented, followed by the measurement taken with the SS RW-14 tube (Figure 4.5) and the SS Swagelok tube (Figure 4.6). Finally, measurement taken with the Ti RW-14 tube are presented.

In all the graphs the heat transfer coefficient is plotted versus the position of the temperature sensors along the tube. The green dotted line is the theoretical prediction made with the Gnielinski equation as is explained in subsection 2.2.1. The red dots are the measured values including, in black, the measurement errors.

(a)

(b)

Heat transfer coefficient water in tube SS RW-12 sHL
$T_f = 15\,[°C]$, $\dot{m} = 21\,[g/s]$, $Q_{eff} = 171W$

Heat transfer coefficient water in tube SS RW-12 sHL
$T_f = 20\,[°C]$, $\dot{m} = 21\,[g/s]$, $Q_{eff} = 172W$

Figure 4.4: Results taken with SS RW-12 of $D_i = 2.16\ mm$ measuring the heat transfer coefficient of water. In 4.4a $T_{fluid} = 15\,°C$ and $Q_{eff} = 171\ W$, in 4.4b $T_{fluid} = 20\,°C$ and $Q_{eff} = 172\ W$. For both graphs $\dot{m} = 21\ g/s$. Large errors arise due to the temperature sensors used, but the results still show that an indication for the heat transfer coefficient of water can be made and thus that the experimental set-up works.

(a)

(b)
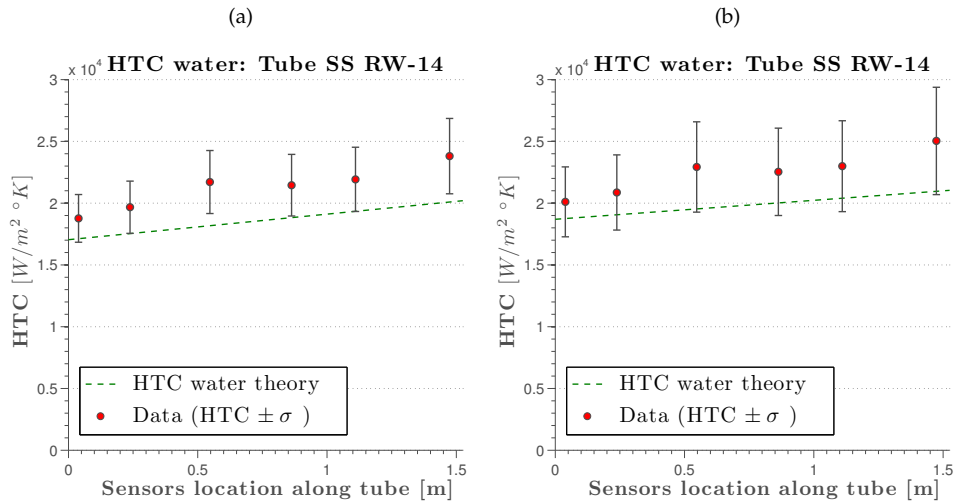
Figure 4.5: Results taken with SS RW-14 of $D_i = 1.6\ mm$ measuring the heat transfer coefficient of water. In 4.5a $T_{fluid} = 15\,°C$ and $Q_{eff} = 307\ W$, in 4.5b $T_{fluid} = 20\,°C$ and $Q_{eff} = 235\ W$. For both graphs $\dot{m} = 7.75\ g/s$. The results again show that an indication for the heat transfer coefficient of water can be made and thus that the experimental set-up works.

(a)

HTC water: Tube Swagelok

(b)

HTC water: Tube Swagelok
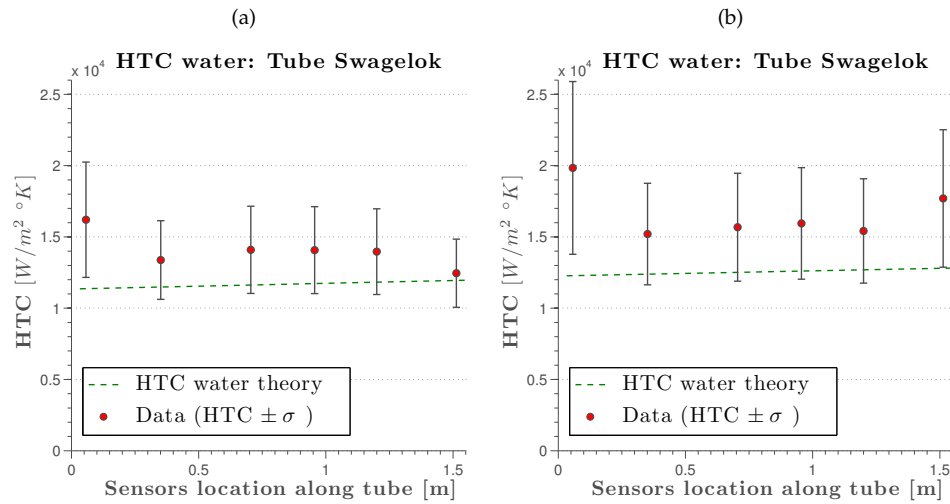
Figure 4.6: Results taken with SS swagelok of $D_i = 4.57\ mm$ measuring the heat transfer coefficient of water. In 4.5a $T_{fluid} = 15\ °C$ and $Q_{eff} = 297\ W$, in 4.5b $T_{fluid} = 20\ °C$ and $Q_{eff} = 297\ W$. For both graphs $\dot{m} = 43\ g/s$. IThe results again show that an indication for the heat transfer coefficient of water can be made and thus that the experimental set-up works.

Data Ti RW-14

(a)

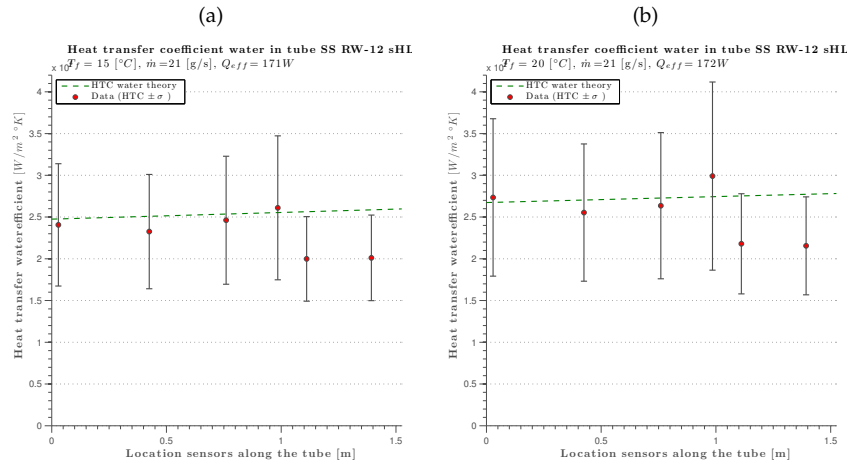**HTC water: Tube Ti RW-14**

(b)

HTC water: Tube Ti RW-14

Figure 4.7: Results taken with Ti RW-14 tube of $D_i = 1.6\ mm$ measuring the heat transfer coefficient of water. In 4.5a $T_{fluid} = 15\ °C$ and $Q_{eff} = 143\ W$, in 4.5b $T_{fluid} = 20\ °C$ and $Q_{eff} = 208\ W$. In both graphs $\dot{m} = 7.5\ g/s$. The results show that an indication for the heat transfer coefficient of water can be made and thus that the experimental set-up works.
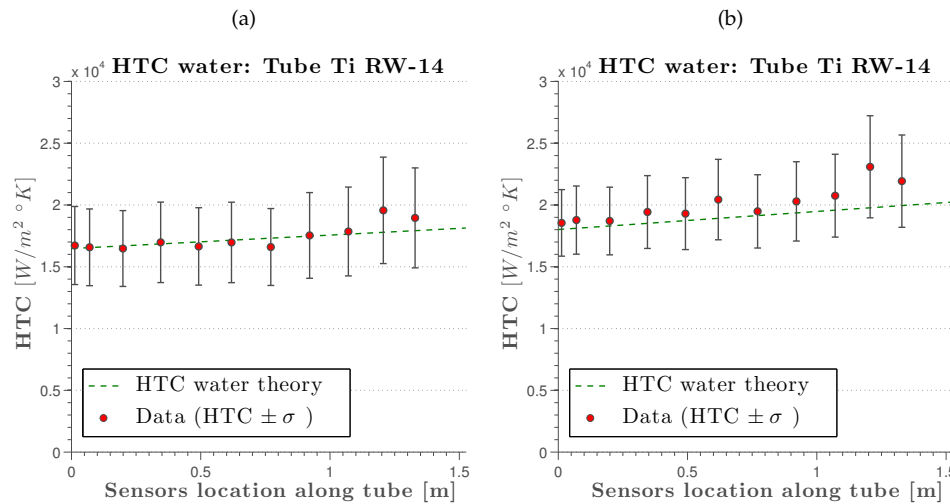
4.2.3 CO_2

Measuring the CO_2 heat transfer coefficient is done in the same way as with water. But, besides varying the heat flux and fluid temperature, now also the influence of the mass flow (between 1 and 4 g/s) is investigated. This creates multiple variables, therefore the strategy is to fix a certain mass flow and use the pressure regulator to set the fluid temperature (between -45 and -15 °C). If this is succeeded a heat flux is applied, then, when the cooling system reaches an equilibrium, a higher heat flux is applied until dry-out is reached. As can be found in Appendix C, the heat transfer coefficient has been determined for a total of 110 different situations. This is to more data that can be presented here, therefore only the most interesting results and data concerning the ATLAS phased upgrade is presented in the following paragraphs.

Tubes

In Figure 4.8 to Figure 4.10 the results for the SS RW-12 tube are presented. In Figure 4.11 to Figure 4.13 the results for the SS RW-14 tube can be found, the Swagelok tube data is presented in Figure 4.14 to Figure 4.15 and finally the data taken with the Ti RW-14 tube is presented in Figure 4.16 to Figure 4.19.

In all graph the heat transfer coefficient is plotted against the vapor quality of the fluid. The green line is the theoretical prediction based on the model of *Thome* [12, 13]. This model predict the heat transfer coefficient with an accuracy of 30%. The measured data is plotted with the red dot surrounded with the errors presented by the black error bars.

Data SS RW-12

In the figures below result concerning the SS RW-12 tube are presented. They compare the influence of the applied heat flux: the left picture has a low power density applied to the tube, while the right picture has a high density applied to the tube. The temperature and mass flux are kept constant per set of graphs.

(a)

Heat Transfer Coefficient CO_2, SS RW-12:
$G = 382.4 \ kg/m^2 \ s$, $q = 5.07 \ kW/m^2$, $T_{sat} = -19.8 \ °C$

(b)

Heat Transfer Coefficient CO_2, SS RW-12:
$G = 353.6 \ kg/m^2 \ s$, $q = 24.5 \ kW/m^2$, $T_{sat} = -18.7 \ °C$

Figure 4.8: Comparison of the predicted heat transfer coefficients to the experimental data taken with the SS RW-12 tube of $D_i = 2.16 \ mm$ at low and high applied heat fluxes. In 4.8a $G = 382.4 \ kg/m^2s$, $q = 5.07 \ kW/m^2$ and $T_{sat} = -19.8$ °C. In 4.8b $G = 353.6 \ kg/m^2s$) and $T_{sat} = -18.7$ °C. Therefore, only the applied heat flux differs from 4.8a and is a factor of 5 higher, $q = 24.5 \ kW/m^2$. This results in a higher average and more flat heat transfer coefficient in the region before dry-out. But, the vapor quality at which dry-out start is decreasing from 0.8 to 0.725, furthermore the highest value in 4.8b is lower then in 4.8a. The data points follow the theoretical prediction well.

In Figure 4.8 the influence of the applied heat flux is strongly noticeable. The heat transfer coefficient is much more flat at a higher heat flux resulting in a better and more stable heat transfer. Furthermore, especially at low vapor quality the increase is enormous (factor of two), while the maximum heat transfer coefficient stays the same.

(a)

Heat Transfer Coefficient CO_2, **SS RW-12:**
$G \leftarrow 400.6 \ kg/m^2$ s, $q = 10.3 \ kW/m^2$, $T_{sat} = -32.3 \ ^\circ C$

(b)

Heat Transfer Coefficient CO_2, **SS RW-12:**
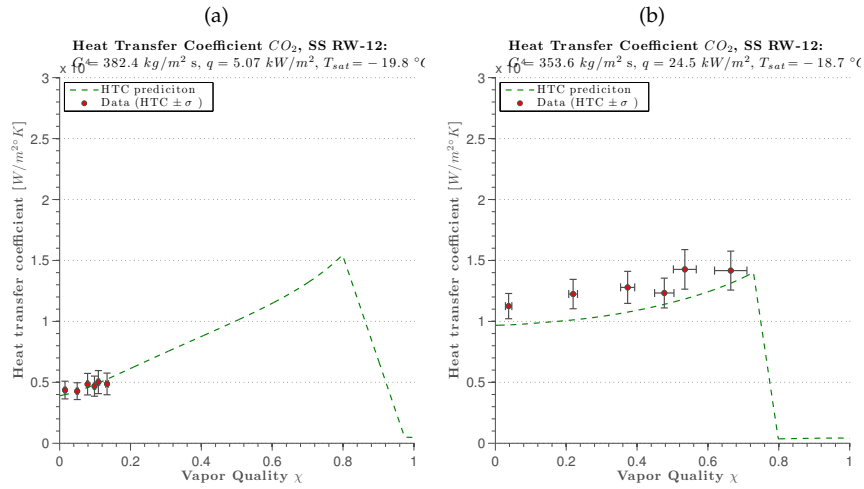$G \leftarrow 468.7 \ kg/m^2$ s, $q = 30.3 \ kW/m^2$, $T_{sat} = -35.1 \ ^\circ C$

Figure 4.9: Comparison of the predicted heat transfer coefficients to the experimental data taken with the SS RW-12 tube of $D_i = 2.16 \ mm$ at low and high applied heat fluxs. In 4.9a $G = 400.6 \ kg/m^2s$, $q = 10.3 \ kW/m^2$ and $T_{sat} = -32.3 \ ^\circ C$, simulation the refrigerating properties of the phased upgrade. In 4.9b $G = 468.7 \ kg/m^2s$ and $T_{sat} = -35.1 \ ^\circ C$. They are thus almost the same as in 4.9a, but the heat flux is a factor 3 higher, $q = 30.3 \ kW/m^2$. This again results in a higher average heat transfer coefficient in the region before dry-out, but now the large increase of the heat transfer coefficient with increasing vapor quality stays. The vapor quality at which dry-out start decreasing more then at low temperatures (Figure 4.8) from 0.76 to 0.65. However, now the maximum value of the heat transfer coefficient, in 4.9b, increases just before dry-out. The data points again follow the theoretical prediction well.

In Figure 4.9, which is at a temperature twice as low as in Figure 4.8 the heat transfer coefficient also increases, especially at low vapor qualities. However, the coefficient increases a factor of two between a vapor quality of zero and the dry-out point.

(a)

Heat Transfer Coefficient CO_2, SS RW-12:
$G = 439.5$ kg/m^2 s, $q = 5.3$ kW/m^2, $T_{sat} = -39.6$ °C

(b)

Heat Transfer Coefficient CO_2, SS RW-12:
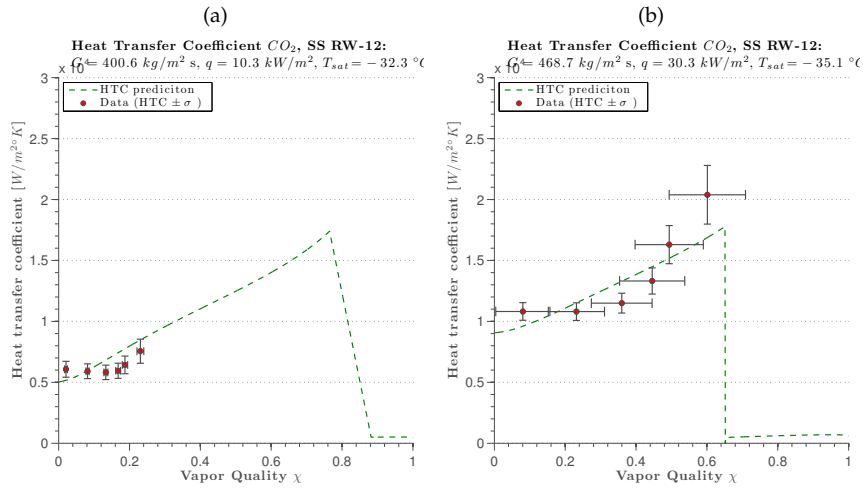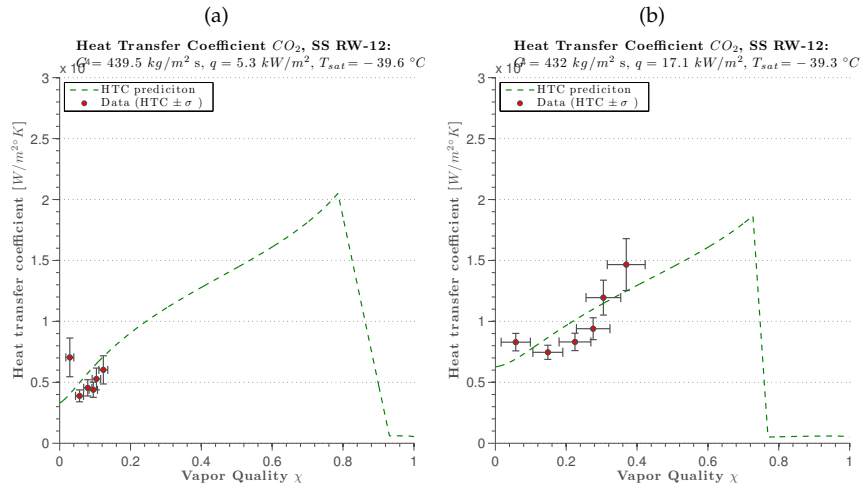$G = 432$ kg/m^2 s, $q = 17.1$ kW/m^2, $T_{sat} = -39.3$ °C

Figure 4.10: Comparison of the predicted heat transfer coefficients to the experimental data taken with the SS RW-12 tube of $D_i = 2.16$ mm at low and high applied heat fluxes. In 4.10a $G = 439.5$ $kg/m^2 s$, $q = 5.3$ kW/m^2 and $T_{sat} = -39.6$ °C. In 4.10b $G = 432$ $kg/m^2 s$ and $T_{sat} = -39.3$ °C). They are the same as in 4.10a, but the heat flux is a factor 3 higher, $q = 17.1$ kW/m^2. Again an increase in the average heat transfer coefficient in the region before dry-out is visible. However, the maximum coefficient is now lower at point of dry-out, just as in 4.10b. Moreover, the theory predicts that the vapor quality at which dry-out starts is the same for both heat fluxes, only the steepness after the dry-out point differs. The data points again follow the theoretical prediction well.

In Figure 4.10, an even colder temperature is reached and the same increase in average heat transfer coefficient is visible as with the two previous graphs. Although this increase is less then at higher temperatures. In all three sets of data, higher heat fluxes do not result in higher heat transfer coefficients at dry-point. Furthermore, if the three left graphs are compared, it is indicated that when the saturation temperate declines the heat transfer coefficient at dry-out point increases. Although, this also could be explained by the variations of mass fluxes. Finally, the vapor quality at which dry-out takes place decreases when the heat flux increases. Hence, a higher average heat transfer coefficient is for a part compensated by a dry-out point at lower vapor quality.s

Data SS RW-14

For the SS RW-14 tube first a comparison with the data of the SS RW-12 is made. Because this is in agreements with the previous section the other graphs show the repeatability of the experiments and the influence of the mass flux on the heat transfer coefficient.

(a)

HTC CO_2: Tube SS RW-14

(b)

HTC CO_2: Tube SS RW-14

Figure 4.11: Comparison of the predicted heat transfer coefficients to the experimental data taken with the SS RW-14 tube of $D_i = 1.6\ mm$ for low and high applied heat flux. In 4.11a $G = 632.7\ kg/m^2s$, $q = 6\ kW/m^2$ and $T_{sat} = -14$ $°C$. In 4.11b $G = 610.1\ kg/m^2s$ and $T_{sat} = -14\ °C$. The heat flux is a factor 4 higher, $q = 24.1\ kW/m^2$. A small decrease in vapor quality at which dry-out starts is visible (0.725 to 0.65). Considering that the green line has a 30% variation, the data points again follow the theoretical prediction well.

Figure 4.11 shows the same behavior as in Figure 4.8 to Figure 4.10: a higher average and more flat heat transfer coefficient in the region before dry-out and a decrease in the maximum coefficient when a higher heat flux is applied.

(a)

HTC CO_2: Tube SS RW-14

(b)

HTC CO_2: Tube SS RW-14

Figure 4.12: Comparison of the predicted heat transfer coefficients to the experimental data taken with the SS RW-14 tube of $D_i = 1.6$ mm for two different measurements at the same experimental settings. In 4.12a $G = 754.5$ kg/m^2s, $q = 11$ kW/m^2 and $T_{sat} = -24.5$ $^{\circ}C$. In 4.12b $G = 739.6$ kg/m^2s, $q = 10.9$ kW/m^2 and $T_{sat} = -24.9$ $^{\circ}C$. The experimental set up values are thus the same, and as visible the data corresponds very well with the theoretical model and with each other.

Although this is the only coinciding data that has been produced during the CO_2 experiments, the reproducibility is surprisingly good.

(a)   (b)
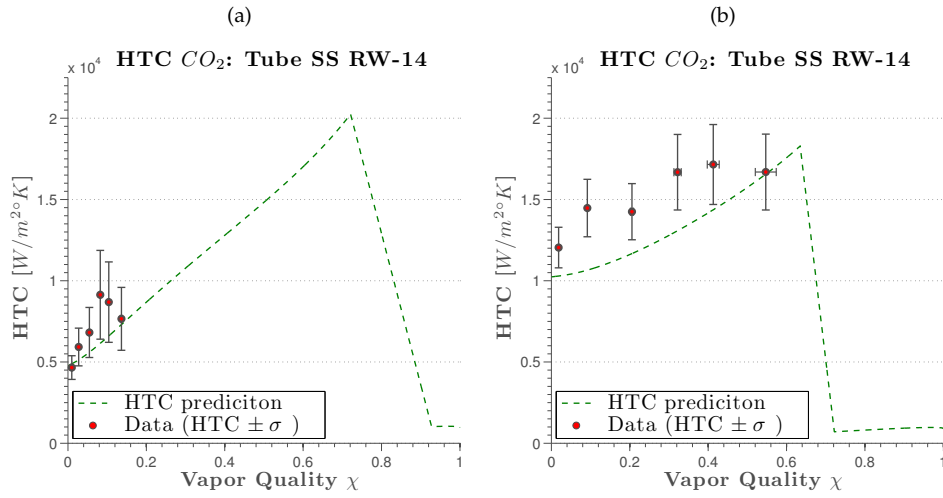

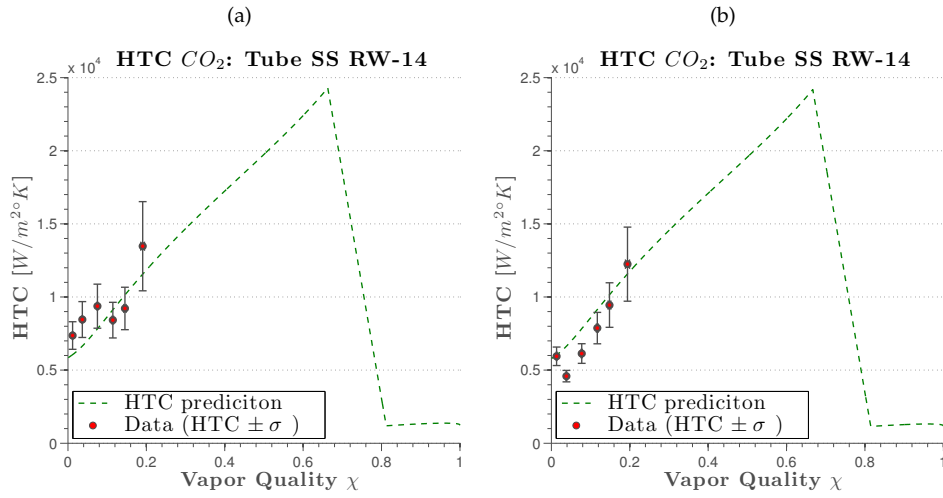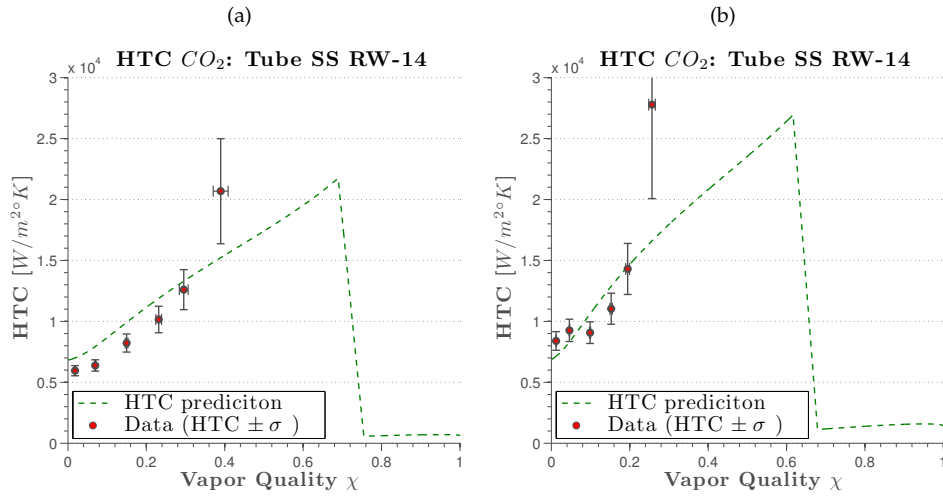
Figure 4.13: Comparison of the predicted heat transfer coefficients to the experimental data taken with the SS RW-14 tube of $D_i = 1.6\ mm$, while variating the mass flux. In 4.13a $G = 546.4\ kg/m^2s$, $q = 17.5\ kW/m^2$ and $T_{sat} = -32.5\ °C$. In 4.13b $G = 824.4\ kg/m^2s$, $q = 17.4\ kW/m^2$ and $T_{sat} = -33\ °C$. The influence of the increasing mass flux is dominant. The maximum heat transfer coefficient increases from 22000 to 27000 while the vapor quality of the data points at the same saturation temperature and the same applied heat flux decreases.

The influence of the mass flux is clearly visualized in Figure 4.13 by the increasing maximum heat transfer coefficient and the decline in vapor quality for the data points at the same saturation temperature and applied heat flux. This implies that at a higher mass flux, the applied heat flux can be increased without reaching dry-out as would be at lower mass fluxes. However, the vapor quality were dry-out arises declines from 0.75 to 0.625.

Data SS Swagelok

The SS Swagelok tube with an inner diameter of $D_i = 4.57\ mm$ has only been measured with low mass fluxes because the blown system is not capable of providing mass flows higher then $5\ g/s$. Therefore, the fluid in the tube is stratified instead of annular flow. As a result, only the bottom of the tube is in contact with liquid, while the top of the tube is in contact with vapor (when the vapor quality is larger then zero). This is due to gravity, but has an influence on the measurement. The temperature sensors are placed at the bottom of the tube to measure the maximum heat transfer coefficient. However, this means that the measured value should be higher then the predicted coefficient because in the theory the average heat transfer coefficient is calculated.

(a) Fig3.

HTC CO_2: Tube Swagelok

(b) $Q = 77.4W$.

HTC CO_2: Tube Swagelok

Figure 4.14: Comparison of the predicted heat transfer coefficients to the experimental data taken with the SS swagelok of $D_i = 4.57\ mm$ for low applied heat flux and varying the mass flux and saturation temperature. In 4.14a $G = 140.5$ $kg/m^2 s$, $q = 9.9\ kW/m^2$ and $T_{sat} = -27.5\ ^\circ C$. In 4.14b $G = 239\ kg/m^2 s$, $q = 10$ kW/m^2 and $T_{sat} = -33\ ^\circ C$. The theoretical prediction is in agreement with the change of mass flux: higher maximum heat transfer coefficient, and dry-out at an earlier stage. The data now falls outside the theoretical prediction, but this is what is expected from the way the measurement have done.

(a) Fig4.   (b) Fig4.

HTC CO_2: Tube Swagelok   **HTC CO_2: Tube Swagelok**
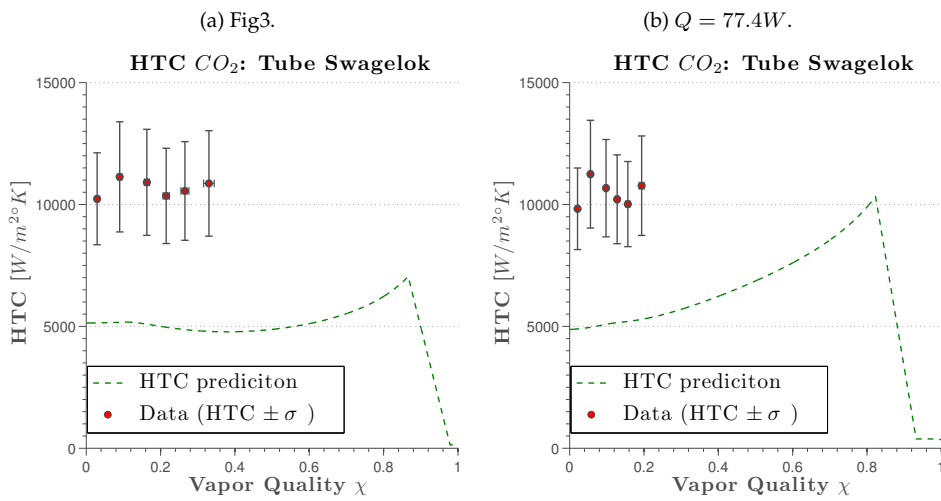
Figure 4.15: Comparison of the predicted heat transfer coefficients to the experimental data taken with the SS swagelok of $D_i = 4.57\ mm$ for medium applied heat flux and varying the mass flux and saturation temperature.. In 4.15a $G = 137\ kg/m^2 s$, $q = 13.6\ kW/m^2$ and $T_{sat} = -27.1\ °C$. In 4.15b $G = 235.6\ kg/m^2 s$, $q = 13.8\ kW/m^2$ and $T_{sat} = -32.8\ °C$. The theoretical prediction predicts, due to a change of mass flux, a higher maximum heat transfer coefficient, and dry-out at an earlier stage. Although again a deviation between prediction and experimental data is visible the shape of the prediction can also be found in the data.

In the four figures the data differs from the theoretical prediction but still follows the profile of the green line. When 4.14b and 4.15b are compared with each other an small decline of the maximum heat transfer coefficient is found. The changing parameter is the applied heat flux.

Data Ti RW-14

The Ti RW-14 tube has the same characteristics as the SS RW-14 tube, except that it is made out of titanium instead of stainless steel. Therefore, first a comparison between the both tubes is made. Then data that compares the influence of the applied heat flux, mass flux and temperature is presented.

(a)

HTC CO_2: Tube Ti RW-14

(b)

HTC CO_2: Tube SS RW-14

Figure 4.16: Comparison of the predicted heat transfer coefficients to the experimental data taken with the Ti RW-14 and SS RW-14 tube both with $D_i = 1.6 \ mm$. Although the experimental values differ slightly: for 4.16a $G = 556.9 \ kg/m^2s$, $q = 20.7 \ kW/m^2$ and $T_{sat} = -31.2 \ °C$; while for 4.16b $G = 546.4 \ kg/m^2s$, $q = 17.5 \ kW/m^2$ and $T_{sat} = -32.5 \ °C$. No deviation due to the tubes material is visible.

(a)

HTC CO_2: Tube Ti RW-14

(b)

HTC CO_2: Tube Ti RW-14
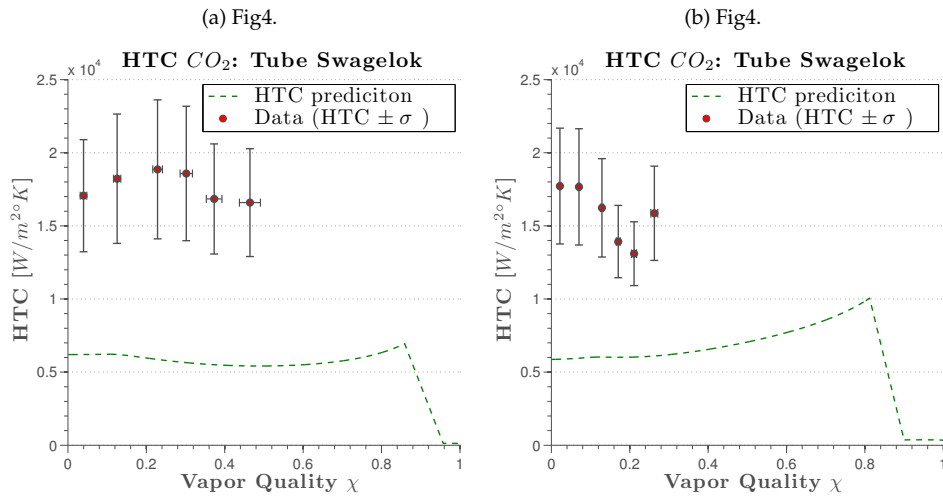

Figure 4.17: Comparison of the predicted heat transfer coefficients to the experimental data taken with the Ti RW-14 of $D_i = 1.6 \ mm$ for low and high applied heat flux. In 4.17a $G = 792.1 \ kg/m^2s$, $q = 8.73 \ kW/m^2$ and $T_{sat} = -24.7 \ °C$. In 4.17b $G = 792.2 \ kg/m^2s$, $q = 19.9 \ kW/m^2$ and $T_{sat} = -23.8 \ °C$. This measurement again confirms the behavior of the heat transfer coefficient of CO_2. When the heat flux increases the average coefficient increases while the maximum coefficient declines and is found at a lower vapor quality.

(a)　　　　　　　　　　　　　　　　　　(b)
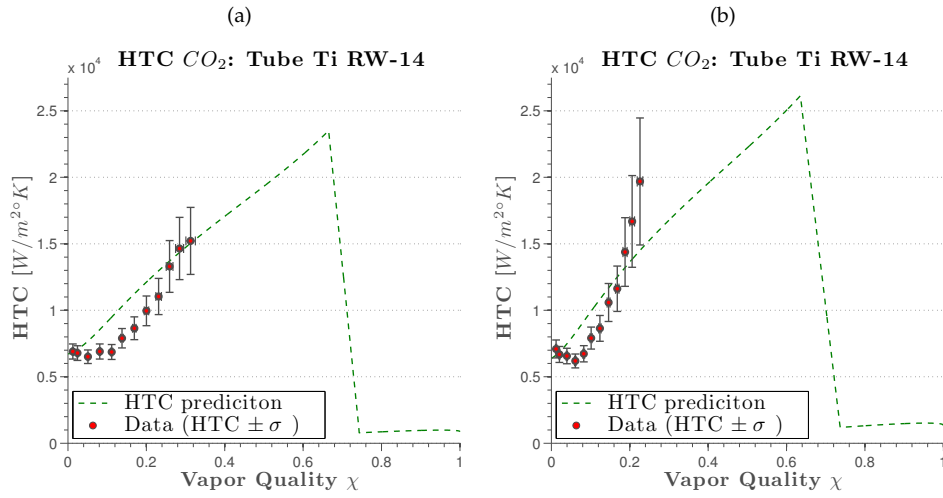
Figure 4.18: Comparison of the predicted heat transfer coefficients to the experimental data taken with the Ti RW-14 of $D_i = 1.6\ mm$ for different mass fluxes. In 4.18a $G = 646.6\ kg/m^2s$, $q = 16.4\ kW/m^2$ and $T_{sat} = -31.2\ °C$. In 4.18b $G = 802.5\ kg/m^2s$, $q = 14.4\ kW/m^2$ and $T_{sat} = -30\ °C$. The influence of the mass flux is mainly the increase in maximum the maximum heat transfer coefficient. Furthermore the vapor quality at which dry-out occurs decrease slightly.
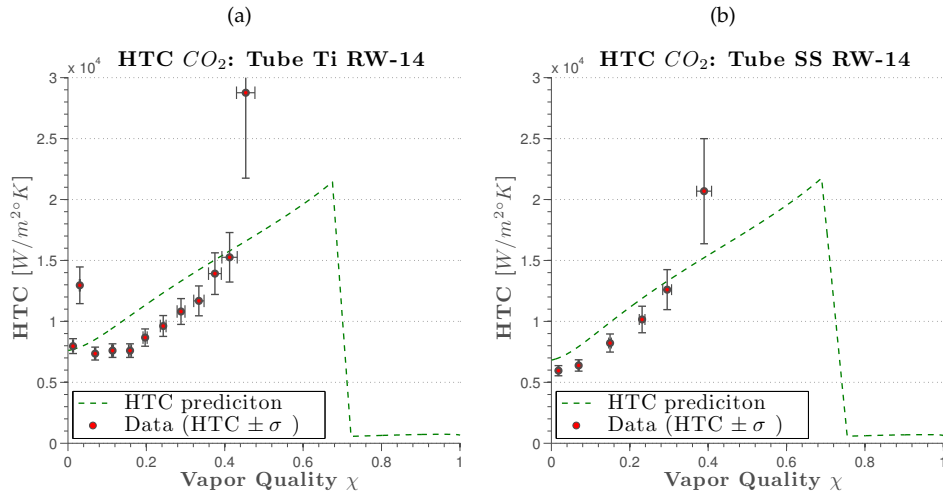
(a)

HTC CO_2: Tube Ti RW-14

(b)

HTC CO_2: Tube Ti RW-14
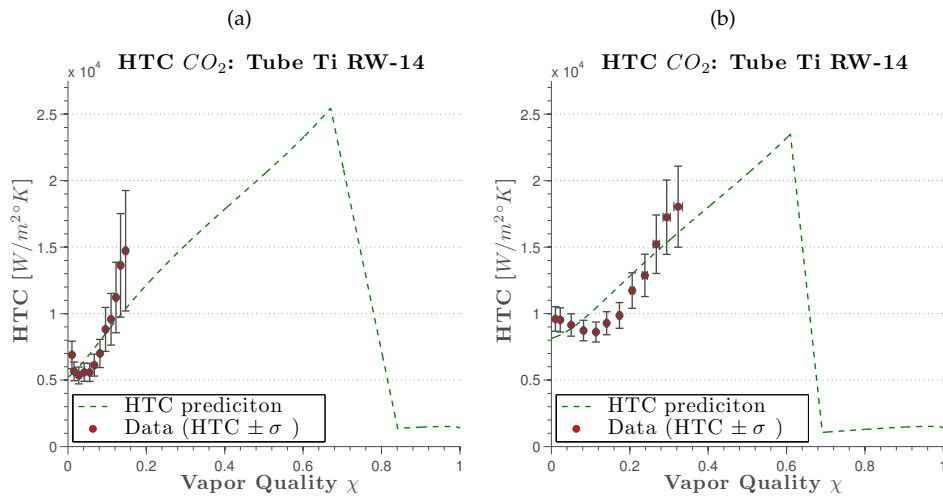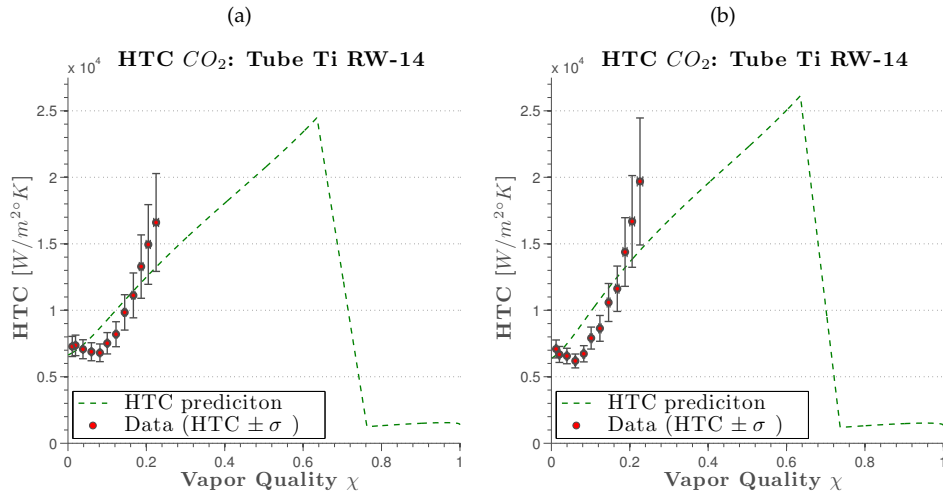

Figure 4.19: Comparison of the predicted heat transfer coefficients to the experimental data taken with the Ti RW-14 of $D_i = 1.6\ mm$ for different saturation temperatures. In 4.19a $G = 801.9\ kg/m^2s$, $q = 13.8\ kW/m^2$ and $T_{sat} = -24.3$ °C. In 4.19b $G = 802.5\ kg/m^2s$, $q = 14.4\ kW/m^2$ and $T_{sat} = -30$ °C. When the saturation temperature becomes lower the maximum heat transfer coefficient increases while the start value at zero vapor quality and the point of dry-out stays the same.

4.2.4 Summary results

Thome model seems to predict the heat transfer coefficient for CO_2 at low temperatures in small diameter tubes well

The implications of this model are:

1. Higher mass flux results in a higher heat transfer coefficient, while the dry-out point starts at a lower vapor quality, but it does not influence the maximum heat transfer coefficient.

2. Lower evaporation temperature results in a higher heat transfer coefficient, without influencing the maximum coefficient and the start of the dry-out.

3. Higher heat flux result in a higher average heat transfer coefficient, the part before dry-out becomes more flat. dry-out is reached at a lower vapor quality.

4.3 Temperature gradient

The temperature gradient along the tube has to be stable, therefore the temperature difference has been measured. The results are presented below for all tubes at different heat fluxes. Because the fluid is evaporating the fluctuations translate directly back to the temperature to the tubes outer wall.
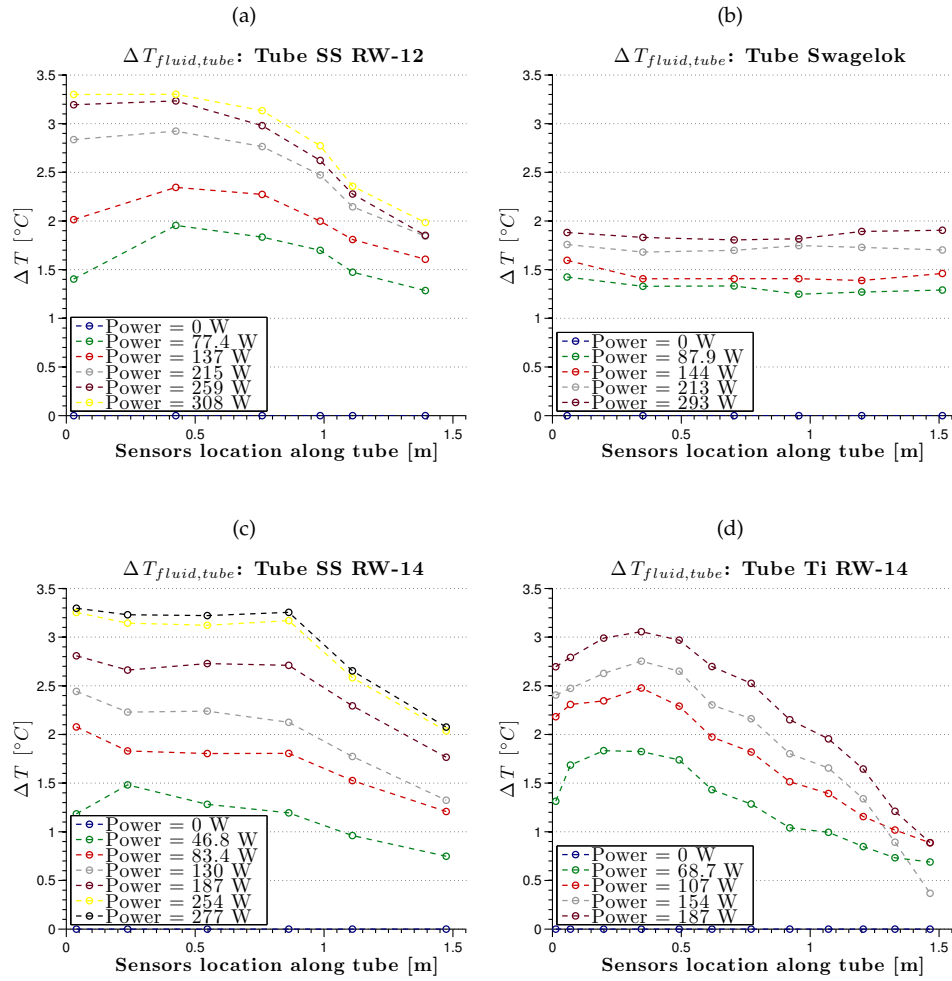
Figure 4.20: Temperature difference between the fluid and outer wall of the tube. Visible in all graphs is the small temperature decline over the tube. which is cause be an increased heat transfer coefficient. In 4.20a $\dot{m} = 1.8\ g/s$ and $T_{sat} = -34$ to -24 (from low to high Q), in 4.20b $\dot{m} = 2.3\ g/s$ and $T_{sat} = -30$, in 4.20a $\dot{m} = 1.5$ g/s and $T_{sat} = 28$ and in 4.20a $\dot{m} = 1.6\ g/s$ and $T_{sat} = -28$. The influence of the tube's material, as far as can be seen from only one single graphs is negligible.

(a)

(b)
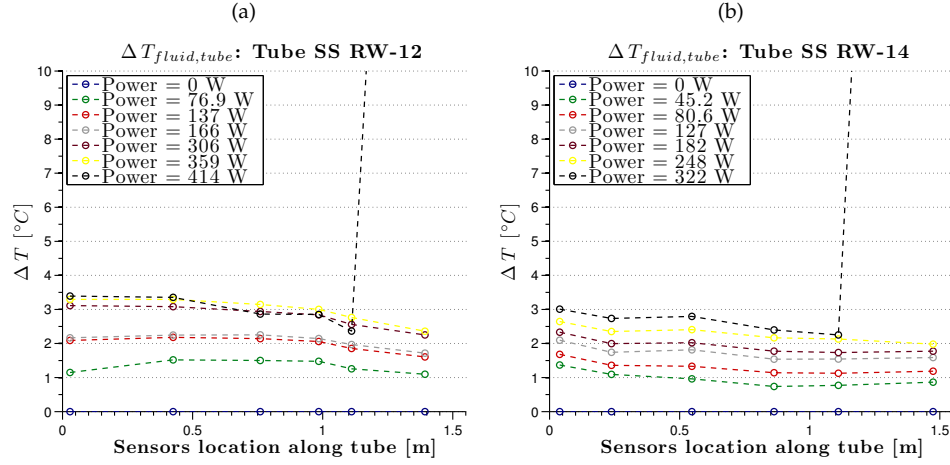
Figure 4.21: Two graphs which show the temperature difference between the fluid and outer wall of the tube. In both graphs dry-out is reached: the black line, which represent a high heat flux, shoots up. The cooling at that point is not sufficient enough anymore, resulting in a rapid incline of the local temperature. In 4.20a $\dot{m} = 2 \ g/s$ and $T_{sat} = -30$ to -24 (from low to high Q), in 4.20b $\dot{m} = 1.3 \ g/s$ and $T_{sat} = -13$.

4.4 Flow maps

4.5 Simulations

4.5.1 Minimum coolant temperature for the phased upgrade

Using the results from subsection 4.2.3, which confirm the Thome model, a prediction for the minimum coolant temperature needed in the phased upgrades can be made. Following section 3.4.1 the total temperature difference can be calculated using Equation 4.1.

$$Q = \frac{\Delta T}{\sum R} \tag{4.1}$$

Considering the found value for the thermal impedance of the Carbon Foam, the sensor temperature, when cooled with CO_2 while applying a certain heat flux, can be calculated using Equation 4.2.

$$T_s = Q \cdot \left[\frac{R_{CF}}{w \cdot l} + \frac{\ln r_2 / r_1}{2\pi k l} + \frac{1}{h_{CO_2} \pi D_i l} \right] + T_f \tag{4.2}$$

The tables in the next two sections contain various options to reach a certain sensor temperature for the specific stave: an effective power is used while variating the saturation temperature of CO_2 and the mass flow, which finally results in the sensor temperature. Also the mass flux, average heat transfer coefficient, vapor quality at the outlet, χ_O, of the tube and the distance, $\Delta \chi_{DO,O}$, between the

vapor quality dry-out point and the vapor quality at the outlet can be found in the tables. This represent a value that indicates if the combination of mass flow and saturation temperature for the tube diameter at an effective power can be used to refrigerate the tube. If $\Delta\chi_{DO,O} < 0.1$ then the dry-out point is to close, or in the case $\Delta\chi_{DO,O} < 0$ would already have been reached. The sensor temperature is then represented with $--$ to indicate that this combination is not an usable option. The margin of 0.1 is used because from the experiments it is know that fluctuation arise, being to close to the dry-out pint thus would result in an unstable system that risks dry-out. Something that may not happen in the detectors.

IBL stave for the phase I upgrade

The characteristics of the stave are: $Q_{nom} = 120\ W$, $Q_{max} = 120\ W$, $D_i = 2\ mm$, $D_o = 2.2\ mm$, $l = 840\ mm$, $w = 20\ mm$, $T_s < -15\ °C$ and $1.0 < \dot{m} < 2.0\ g/s$. The titanium tube has a thermal coefficient $k_{tube} = 21.9\ W/m°K$. The thermal impedance of the Carbon Foam has been measured at $R_{CF} = 11.62\ °Kcm^2/W$, however, the value aimed for is $R_{CF} = 5\ °Kcm^2/W$. In the tables, therefore simulations for both values have been made.

Q [W]	T_{sat} [°C]	$\dot{m}$ [g/s]	**G** [kg/m²]	χ_{Out} [kJ/kg]	$\Delta\chi_{DO,O}$	$< h_{CO_2} >$ [W/m²°K]	T_s [°C] $R = 11.62$	T_s [°C] $R = 5$
80	-25	1.0	318.3	0.473	0.300	8882	-17.69	-20.85
80	-25	1.5	477.5	0.382	0.335	10417	-17.95	-21.10
80	-25	2.0	636.6	0.336	0.335	11973	-18.13	-21.29
80	-30	1.0	318.3	0.564	0.310	9085	-22.73	-25.88
80	-30	1.5	477.5	0.376	0.343	10906	-23.01	-26.16
80	-30	2.0	636.6	0.332	0.342	12708	-23.21	-26.36
80	-35	1.0	318.3	0.455	0.320	9389	-27.79	-30.94
80	-35	1.5	477.5	0.370	0.350	11498	-28.08	-31.23
80	-35	2.0	636.6	0.328	0.347	13546	-28.28	-31.43

Table 4.1: Simulation results for the IBL prototype stave. The sensor temperature has been calculated for different mass flows and saturation temperatures with CO_2 as refrigerant in a tube of $D_i = 2\ mm$, and a power dissipation of $80\ W$. Calculations have been done for the measured and the aimed value of the Carbon Foam's thermal impedance. It is assumed that the vapor quality at the inlet of the tube is $\chi_{In} = 0.2$, because at the used mass fluxes then annular flow can be assumed. $\Delta\chi_{DO,O}$ is the vapor quality left between χ_{Out} and the vapor quality dry-out point.

For nominal power dissipation CO_2 seems to be an excellent coolant. Already at saturation temperatures of $-25\ °C$ and a mass flow of $1.0\ g/s$ sufficient cooling is reached.

Q [W]	T_{sat} [°C]	$\dot{m}$ [g/s]	**G** [kg/m²]	χ_{Out} [kJ/kg]	$\Delta\chi_{DO,O}$	$<h_{CO_2}>$ [W/m²°K]	T_s [°C] $R = 11.62$	T_s [°C] $R = 5$
120	-25	1.0	318.3	0.609	0.143	10528	-14.44	-19.17
120	-25	1.5	477.5	0.473	0.219	11863	-14.68	-19.41
120	-25	2.0	636.6	0.205	0.238	13266	-14.89	-19.62
120	-30	1.0	318.3	0.595	0.159	10601	-19.46	-24.18
120	-30	1.5	477.5	0.464	0.230	12219	-19.74	-24.47
120	-30	2.0	636.6	0.398	0.247	13872	-19.96	-24.69
120	-35	1.0	318.3	0.583	0.172	10790	-24.49	-29.22
120	-35	1.5	477.5	0.455	0.2401	12695	-24.81	-29.54
120	-35	2.0	636.6	0.392	0.254	14609	-25.04	-29.77

Table 4.2: Simulation results for the IBL prototype stave. The sensor temperature has been calculated for different mass flows and saturation temperatures with CO_2 as refrigerant in a tube of $D_i = 2\ mm$, and a power dissipation of $120\ W$. Calculations have been done for the measured and the aimed value of the Carbon Foam's thermal impedance. It is assumed that the vapor quality at the inlet of the tube is $\chi_{In} = 0.2$, because at the used mass fluxes then annular flow can be assumed. $\Delta\chi_{DO,O}$ is the vapor quality left between χ_{Out} and the vapor quality dry-out point.

For maximum power dissipation again CO_2 is an excellent coolant. Although the first entry comes closer to dry-out the cooling is is still sufficient. In Figure 4.22 the corresponding heat transfer coefficients of Table 4.3 are shown. With two dots the vapor quality at the inlet and outlet are visualized.
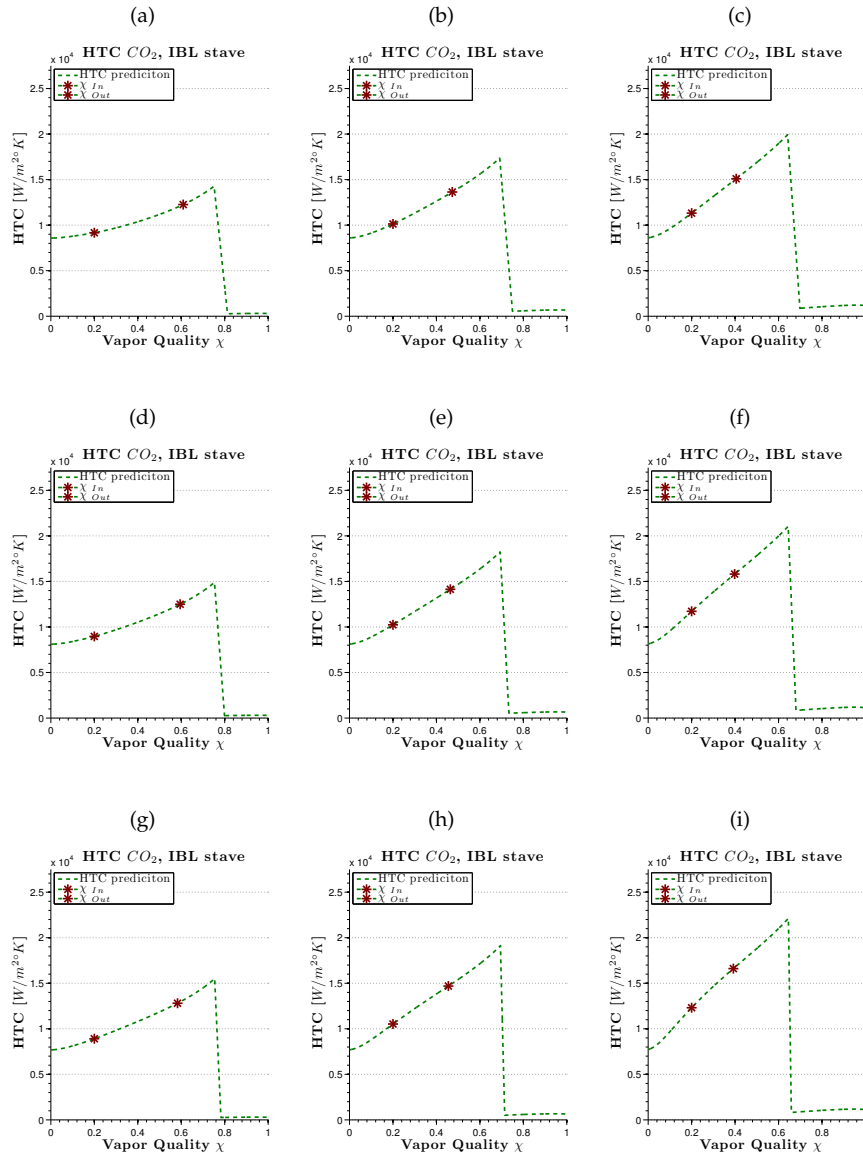
Figure 4.22: Heat transfer coefficient graphs that correspond with Table 4.3. From top to bottom the temperature decreases ($-5\ ^\circ C$), and from left to right the mass flow increase ($0.5\ g/s$). The two dots represent the vapor quality at the inlet and outlet of the simulated stave.

The heat transfer coefficient graphs show no dry-out in the operating range, it is therefore interesting to know if also a smaller tube can be used. This would mean a minimization of the material needed that will reduce multiple scattering. In Table 4.3 the situations of Figure 4.22 are repeated only now with a tube of $D_i = 1.5\ mm$.

Q [W]	T_{sat} [°C]	$\dot{m}$ [g/s]	**G** [kg/m²]	χ_{Out} [kJ/kg]	$\Delta\chi_{DO.O}$	$<h_{CO_2}>$ [W/m²°K]	T_s [°C] $R = 11.62$	T_s [°C] $R = 5$
120	-25	1.0	565.8	0.509	0.134	14067	-14.42	-19.14
120	-25	1.5	848.3	0.373	0.191	15677	-14.64	-19.36
120	-25	2.0	1131.8	0.305	0.196	17264	-14.81	-19.54
120	-30	1.0	565.8	0.495	0.142	14389	-19.46	-24.19
120	-30	1.5	848.3	0.364	0.184	16348	-19.72	-24.44
120	-30	2.0	1131.8	0.298	0.182	18225	-19.91	-24.64
120	-35	1.0	565.8	0.483	0.131	14864	-24.53	-29.26
120	-35	1.5	848.3	0.355	0.168	17180	-24.81	-29.53
120	-35	2.0	1131.8	0.292	0.162	19387	-25.01	-29.73

Table 4.3: Simulation results for the IBL prototype stave. The sensor temperature has been calculated for different mass flows and saturation temperatures with CO_2 as refrigerant in a tube of $D_i = 1.5\ mm$, and a power dissipation of $120\ W$. Calculations have been done for the measured and the aimed value of the Carbon Foam's thermal impedance. It is assumed that the vapor quality at the inlet of the tube is $\chi_{In} = 0.1$, instead of $\chi_{In} = 0.2$ to increase the region before dry-out. Annular flow still can be assumed. $\Delta\chi_{DO,O}$ is the vapor quality left between χ_{Out} and the vapor quality dry-out point.

Although the value of $\chi_{In} = 0.1$ is now lower, CO_2 is still an excellent coolant. Hence, it could be an option to reduce the refrigerant tube to $1.5\ mm$, because it meets all the criteria for the IBL upgrade.

Outer Pixel stave for the sLHC

For the sLHC upgrade simulation for the Outer Pixel Staves can also be made using Equation 4.2. The characteristics of the prototype stave are: $Q_{nom} = 200\ W$, $Q_{max} = 300\ W$, $D_i = 2\ mm$, $D_o = 2.2\ mm$, $l = 1500\ mm$, $w = 40\ mm$, $T_s < -15\ °C$ and $1.0 < \dot{m} < 2.0\ g/s$. The tube and supporting structure material stay the same, that is, titanium and carbon foam respectively. Therefore $R_{CF} = 5\ °Kcm^2/W$ and $k_{tube} = 21.9\ W/m°K$. The value of R is the value that is reached with finite element methods. However, Carbon Foam at this quality is at the moment not yet fabricated. Because the phase II upgrade is still more then 10 years away it is assumed that R&D will solve the problems that are arising at the moment with the fabrication of Carbon Foam and will succeed in lowering the thermal impedance to, or even below, $5\ °Kcm^2/W$.

Q [W]	T_{sat} [°C]	$\dot{m}$ [g/s]	G [kg/m²]	χ_{Out} [kJ/kg]	$\Delta\chi_{DO,O}$	$< h_{CO_2} >$ [W/m²°K]	T_s [°C] R = 5
200	-30	1.5	477.5	0.539	0.209	11895	-26.46
200	-30	2.0	636.6	0.430	0.235	12985	-26.61
200	-30	2.5	795.77	0.364	0.244	14042	-26.73
200	-30	3.0	954.9	0.320	0.161	15066	-26.83
200	-35	1.5	477.5	0.526	0.222	12294	-31.51
200	-35	2.0	636.6	0.419	0.230	13577	-31.68
200	-35	2.5	795.77	0.355	0.245	14814	-31.81
200	-35	3.0	954.9	0.313	0.253	16012	-31.92
200	-40	1.5	477.5	0.514	0.174	12787	-36.58
200	-40	2.0	636.6	0.410	0.230	14288	-36.76
200	-40	2.5	795.77	0.348	0.247	15722	-36.89
200	-40	3.0	954.9	0.307	0.248	17093	-37.00

Table 4.4: Simulation results for the SCT prototype stave. The sensor temperature has been calculated for different mass flows and saturation temperatures when CO_2 is used as refrigerant in a tube $D_i = 2\ mm$ and a heat flux of 200 W. Calculations have been done for the aimed value of the Carbon Foam's thermal impedance. It is assumed that the vapor quality at the inlet of the tube equals $\chi_{In} = 0.1$.

At nominal effective power CO_2 seems to be an excellent coolant. Under all situations is it capable of cooling the sensors below $-15\ °C$ without reaching the dry-out point.

Q [W]	T_{sat} [°C]	$\dot{m}$ [g/s]	G [kg/m²]	$\Delta\chi$ [kJ/kg]	$\Delta\chi_D - \chi_{max}$	$< h_{CO_2} >$ [W/m²°K]	T_s [°C] R = 5
300	-30	1.5	477.5	0.782	-0.123	11354	–
300	-30	2.0	636.6	0.612	-0.013	15079	–
300	-30	2.5	795.77	0.509	0.040	16544	–
300	-30	3.0	954.9	0.441	0.065	17511	–
300	-35	1.5	477.5	0.759	-0.122	11461	–
300	-35	2.0	636.6	0.594	-0.019	15244	–
300	-35	2.5	795.77	0.495	0.028	17216	–
300	-35	3.0	954.9	0.430	0.051	18370	–
300	-40	1.5	477.5	0.7386	-0.128	11469	–
300	-40	2.0	636.6	0.579	-0.033	15184	–
300	-40	2.5	795.77	0.483	0.011	18014	–
300	-40	3.0	954.9	0.419	0.031	19340	–

Table 4.5: Simulation results for the SCT prototype stave. The sensor temperature has been calculated for different mass flows and saturation temperatures when CO_2 is used as refrigerant in a tube $D_i = 2\ mm$ and a heat flux of 300 W. Calculations have been done for the aimed value of the Carbon Foam's thermal impedance. It is assumed that the vapor quality at the inlet of the tube equals $\chi_{In} = 0.1$.

In Table 4.5 simulation concerning a tube of $2\ mm$ under a effective power of $300\ W$ are presented. There are now situation to effectively cool the sensors without reaching dry-out in the tube. This is visualized in Figure 4.23 where the twelve heat transfer coefficient graphs are shown, with the two dots marking the inlet and outlet vapor quality. Because this tube size is not an option under the applied conditions the influence of a larger tubes diameter is investigated in Table 4.6 with $D_i = 2.5\ mm$.
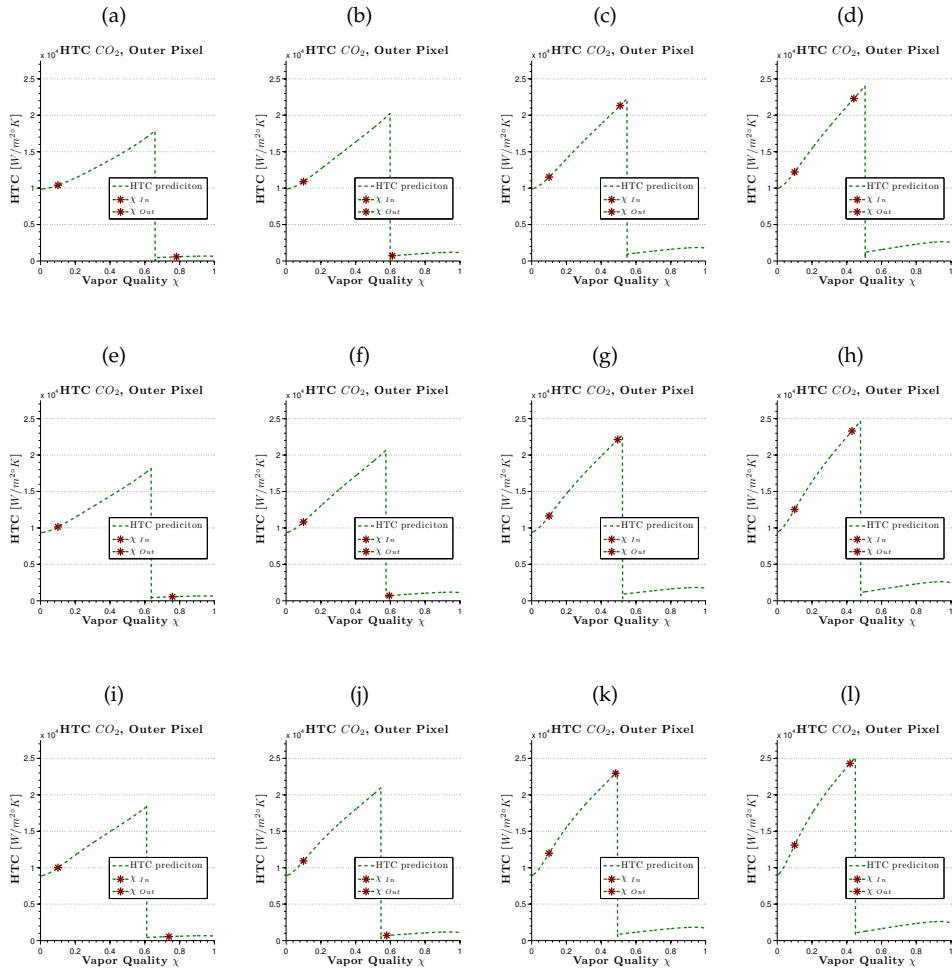
(a) (b) (c) (d)

(e) (f) (g) (h)

(i) (j) (k) (l)

Figure 4.23: Heat transfer coefficient graphs that correspond with Table 4.5. From top to bottom the temperature decreases ($-5\,°C$), and from left to right the mass flow increase ($0.5\,g/s$). The two dots represent the vapor quality at the inlet and outlet of the simulated stave.

Q	T_{sat}	$\dot{m}$	G	$\Delta\chi$	$\Delta\chi_D - \chi_{max}$	$< h_{CO_2} >$	T_s [°C]
[W]	[°C]	[g/s]	[kg/m²]	[kJ/kg]		[W/m²°K]	$D_i = 1.5(2.5)$ mm
300	-30	1.5	477.5	0.782	-0.0290	10501	–
300	-30	2.0	636.6	0.612	0.101	11298	-25.1342
300	-30	2.5	795.77	0.509	0.167	11895	-25.25
300	-30	3.0	954.9	0.441	0.203	12496	-25.35
300	-35	1.5	477.5	0.759	-0.005	10767	–
300	-35	2.0	636.6	0.594	0.119	11452	-30.16
300	-35	2.5	795.77	0.495	0.180	12175	-30.30
300	-35	3.0	954.9	0.430	0.210	12905	-30.41
300	-40	1.5	477.5	0.7386	0.007	10895	–
300	-40	2.0	636.6	0.579	0.115	11706	-35.21
300	-40	2.5	795.77	0.483	0.168	12571	-35.36
300	-40	3.0	954.9	0.419	0.193	13424	-35.49

Table 4.6: Simulation results for the SCT prototype stave. The sensor temperature has been calculated for different mass flows and saturation temperatures when CO_2 is used as refrigerant in a tube $D_i = 2.5$ mm and a heat flux of 300 W. Calculations have been done for the aimed value of the Carbon Foam's thermal impedance. It is assumed that the vapor quality at the inlet of the tube equals 0.1, this the lowest quality were annular flow still can be assumed.

Hence, a tube with larger diameter could be a solution to the problem, although it is then a compromise between the used mass flow and the material needed for the tube. The same does not apply for smaller tubes, although the heat transfer coefficient then increases, the dry-out is reached in all situation, resulting in poor cooling performances.

4.6 Infrared camara

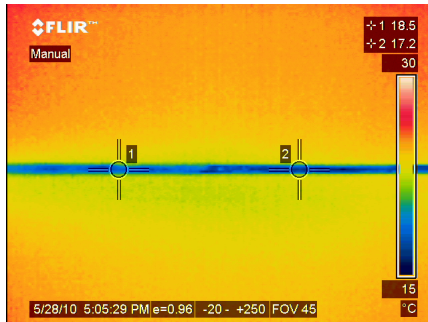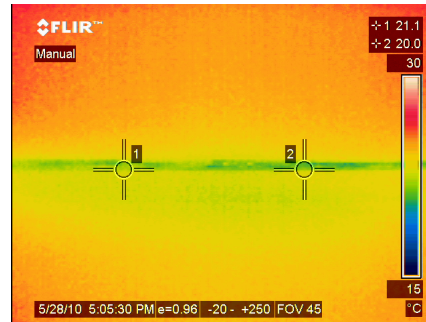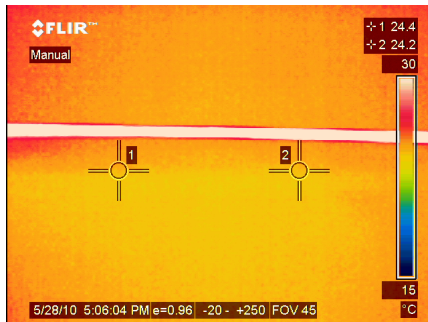In Figure 4.24 four pictures are shown.

(a) Infrared snapshot of SS RW-12: cooled with water at a temperature of 15 $^\circ C$.

(b) Infrared snapshot of SS RW-12: cooled with water at $T = 15\,^\circ C$ and $330W$ applied.

(c) Infrared snapshot of SS RW-12: not cooled while $330W$ of heat is applied.

(d) Infrared snapshot of SS RW-12: with $330W$ applied, but now cooled again.
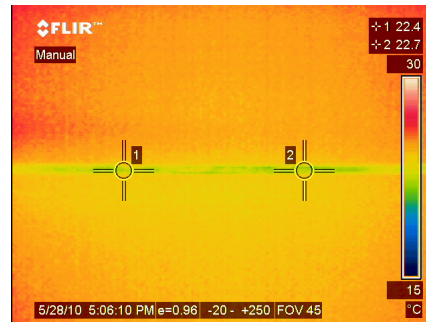
Figure 4.24: Four snapshot from a infrared camera movie, where first a tube is refrigerated (water), subsequently a $330W$ power is applied, then the cooling is paused, and finally the cooling is put back on.

To determine the heat transfer coefficient of CO_2, temperature sensors are attached along a small diameter tube. When evaporative CO_2 at a certain mass flow ($\dot{m}$) or mass flux ($G = \frac{4 \cdot \dot{m}}{\pi D_i^2}$) flows through the tube a current is applied over the tube's wall. Due to (the small) resistance of the tube the metal heats up. Better said, a heat flux is applied when a current flows through the tubes wall. The CO_2 will absorb (a part) of the heat and the sensors along the tube will measure the temperature of the outer wall. At the same time the temperature of the fluid is determined by pressure sensors at the inlet and outlet of the tube. This is possible because the fluid is evaporating. Hence, a certain pressure equals a certain temperature. Using the right equations, the ΔT between the inner wall and fluid can be determined. Because R_{tube} can be measured and the value of I is a constant in a circuit in series, Q_{eff} is known and the heat transfer coefficient can be calculated.

Chapter 5

Conclusions & Discussion

5.1 Conclusions

5.2 Discussion

The limitation of the blown system become visible when the vapor quality becomes larger then the dry-out region. Then the heat transfer of CO_2 reduced rapidly and the pre-cooling system stops working, therefore the vapor quality at the inlet of the tube increases and the system reaches a viscus circle.

5.3 Recommendations

Something about: investigating dry-out point -¿ no stable pre-cooling at the moment Keeping the temperature for the sensors as constant as possible by variating mass flow and vapor quality (now only started with 0 %)

Bibliography

[1] (2010 May). CERN in a Nutshell. Retrieved May 28th 2010, from http://public.web.cern.ch/public/en/About/About-en.html.

[2] CERN-Press-office (2009 November 30th). LHC sets new world record. Retrieved June 8th, 2010, from http://press.web.cern.ch/press/PressReleases/Releases2009/PR18.09E.html.

[3] CERN-Press-office (2010 March 30th). LHC research programme gets underway. Retrieved May 29th, 2010, from http://press.web.cern.ch/press/PressReleases/Releases2010/PR07.10E.html.

[4] ATLAS-Collaboration (2010). ATLAS Fact Sheet. Technical report, CERN, Geneva. Retrieved May 26th, 2010, from http://www.atlas.ch/.

[5] Darbo, G. (2010 February). The ATLAS IBL project. Slides.

[6] Flick, T. (2009 September). IBL - ATLAS Pixel Upgrade. *Proceedings of Science*.

[7] Capeans, M., & Einsweiler, K. (2010 March 3th). ATLAS Insertable B-layer Technical Design Repor. *To be submitted to: LHCC*.

[8] Oriunno, M., Battistin, M., David, E., et al. (2007). Design and prototype studies of the TOTEM Roman pot detectors. *Nuclear Instruments and Methods in Physics Research A*, *581*, 499–503.

[9] Attree, D., & et al. (2008 July). The evaporative cooling system for the ATLAS inner detector. *Institute of Physics Publishing and Sissa*.

[10] Verlaat, B. (2002). Feasibility Demonstration of a Mechanically Pumped Two-Phase CO2 Cooling Loop for the AMS-2 Tracker Experiment. *Conference on Thermophysics in Microgravity, in the Space Technology & Applications International Forum (STAIF-2002)*. Albuquerque, NM, USA.

[11] Verlaat, B. (2007). Controlling a 2-phase CO2 loop using a 2-phase accumulator. *International Congress of Refrigeration 2007*. Beijing.

[12] Cheng, L., Ribatski, G., Quibén, J. M., & Thome, J. R. (2008). New prediction methods for CO2 evaporation inside tubes: Part I – A two-phase flow pattern map and a flow pattern based phenomenological model for two-phase flow frictional pressure drops. *International Journal of Heat and Mass Transfer*, (51), 111–124.

[13] Cheng, L., Ribatski, G., Quibén, J. M., & Thome, J. R. (2008). New prediction methods for CO2 evaporation inside tubes: Part II—An updated general flow boiling heat transfer model based on flow patterns. *International Journal of Heat and Mass Transfer*, (51), 125–135.

[14] Feld, L., Glessing, W., & Hammarström, R. (1998 February 23th). Thermal Properties of the Silicon Microstrop Endcap Detector. *CMS Note*, *018*, 1–16.

[15] Pernegger, H. (2009). Sensor temperature and thermal run-away estimate IBL. Technical report, CERN.

[16] Kenney, C. (2006 April 5th). Active Edge and 3D Sensors. International symposium on detector development, SLAC National Accelerator Laboratorium.

[17] Incropere, F., DeWitt, D., Bergman, T., & Lavine, A. (2007). *Fundamentals of Heat and Mass Transfer*. Hoboken, NJ: John Wiley and Sons, 6th edition.

[18] Munson, B., Young, D., & Okiishi, T. (2006). *Fundamentals of Fluid Mechanics*. Hoboken, NJ: John Wiley and Sons, 5th edition.

[19] Zürcher, O., Thome, J., & Favrat, D. (1999 February). Evaporation of Ammonia in a Smooth Horizontal Tube: Heat Transfer Measurements and Predictions. *Journal of Heat Transfer*, *Vol. 121*, 89–101.

[20] Kattan, N., Thome, J. R., & Favrat, D. (1998 February). Flow Boiling in Horizontal Tubes: Part 1 – Development of a Diabatic Two-Phase Flow Pattern Map. *Journal of Heat Transfer*, *Vol. 120*, 140–147.

[21] Kattan, N., Thome, J. R., & Favrat, D. (1998 February). Flow Boiling in Horizontal Tubes: Part 2 – New Heat Transfer Data for Five Refrigerants. *Journal of Heat Transfer*, *Vol. 120*, 148–155.

[22] Kattan, N., Thome, J. R., & Favrat, D. (1998 February). Flow Boiling in Horizontal Tubes: Part 3 – Development of a New Heat Transfer Model Based on Flow Pattern. *Journal of Heat Transfer*, *Vol. 120*, 156–165.

[23] Bejan, A., & Kraus, A. D. (2003). *Heat Transfer Handbook*. Chapter 9, Hoboken, NJ: John Wiley and Sons, 1st edition.

[24] Wojtan, L., Ursenbacher, T., & Thome, J. R. (2005). Inverstigation of flow boiling in horizontal tubes: Part I–A new diabatic two-phase flow pattern map. *International Journal of Heat and Mass Transfer*, (48), 2955–2969.

[25] Fox, J. N. (1990). Temperature coefficient of resistance. *Phys. Educ*, *25*, 167–169.

[26] US_Secretary_of_Commerce (2008). NIST database. Retrieved between March and May 2010, from http://webbook.nist.gov/chemistry/fluid/.

[27] New England Small Tube. Http://www.nesmalltube.com/index.html. Litchfield Technology Park, 480 Charles Bancroft Hwy., Litchfield, NH 03052, U.S.A.

[28] Swagelok. Http://www.swagelok.com/default.aspx. Sunnyvale, CA 94089, 929 Weddell Court, U.S.A.

[29] Deacon, C. G. (1992 Sept.). Error Analysis in the Introductory Physics Laboratory. *The Physics Teacher*, 30, 368–370.

[30] de Wolf, E. (2009 September). Statistical Data Analysis. Printed.

Appendix A

Nomenclature

Normal

A = cross-sectional area, m^2
D = tube diameter, m^2
f = volume flow, m^3/s
G = total fluids mass velocity, kg/sm^2
g = gravitational constant, m/s^2
h = heat transfer coefficient, W/m^2
I = current, A
l = length of tube, m
k = Boltzmanns constant, $8.6210^{-5}\ eV/^\circ K$
$\dot{m}$ = mass flow, kg/s
P = pressure Pa
Q = applied power, W
q = power density $q = Q/A$, W/m^2
R = thermal impedance $^\circ K cm^2/W$
T = temperature, $^\circ C$
U = voltage, V
w = width resistor, m

Greek Symbols

α = temperature coefficient, $^\circ K^{-1}$
κ = leakage current damage constant, A/cm
ρ = density, kg/m^3
σ = surface tension, N/m
Φ = particle fluence
μ = dynamic viscosity, $Pa \cdot s$
ν = kinematic viscosity, Ns/m^2
χ = vapor quality, %

Table A.1: Overview of used electronic device that have relevant errors, with FS full scale and T the temperature [$^\circ C$].

A = cross-sectional area, m^2

D = tube diameter, m^2

f = volume flow, m^3/s

G = total fluids mass velocity, kg/sm^2

g = gravitational constant, m/s^2

h = heat transfer coefficient, W/m^2

I = current, A

l = length of tube, m

k = Boltzmanns constant, $8.62 10^{-5}\ eV/^{\circ}K$

$\dot{m}$ = mass flow, kg/s

P = pressure Pa

Q = applied power, W

q = power density $q = Q/A$, W/m^2

R = thermal impedance $^{\circ}K cm^2/W$

T = temperature, $^{\circ}C$

U = voltage, V

w = width resistor, m

Greek symbols

α = temperature coefficient, $^{\circ}K^{-1}$

κ = leakage current damage constant, A/cm ρ = density, kg/m^3

σ = surface tension, N/m

Φ = particle fluence

μ = dynamic viscosity, $Pa \cdot s$

ν = kinematic viscosity, Ns/m^2

χ = vapor quality, %

Dimensionless Numbers

f = friction factor

Pr = Prandtl number $[C_p \mu / k]$

Re = Reynolds number $[4\dot{m}/\pi\mu D_i]$

Subscripts

D = dimensionless

CO_2 = carbon dioxide

f = fluid or coolant

i = inner

o = outer

r = resistor

ref = reference

s = sensor

Si = silicon

w = wall

p = dat ding van heat capacity

Appendix B

MATLAB DAQ Program Manual

B.1 Adding a New Measurement

When a new file is recorded with Labview, open it with a plain text program like Notepad. Remove the header and save the file. Subsequently import the file in Excel and save it as a windows comma separated file (extension .csv). Save this file in the data map of MATLAB.

Depending if the new measurement has been done with water or CO_2 open: $water\_info\_tubes.m$ or $co2\_info\_tubes.m$. For each tube there is a case which contains the specific data. Fill the file name of the new measurement in $files = \{\}$, use $'$ at the start and end of the file name. Furthermore, fill in all the details as inner tube diameter, outer tube diameter, location of the sensors (do not forget the includes the in and outlet sensors (they are placed at 0 and at the length of tube) and total resistance of the tube. Save the file and open $New\_DAQ.m$. Run the file and follow the options in the terminal: Choose first which kind of analyze has to be done and secondly which tube/stave has to be used, the interface is shown in Listing B.1.

Listing B.1: Interface Matlab program

```
Which program do you want to run?
− 1 is Thermal Impedance (IBL stave)
− 2 is Thermal Impedance incl HTC (IBL stave)
− 3 is Bare stave water measurement
− 4 is Bare stave HTC
− 5 is HTC simulation
run program:

For which tube do you want this program to run?
− 1 is IBL stave
− 2 is LBNL stave
− 3 is SS RW−12 IBL
− 4 is SS RW−12 sHLC
− 5 is SS RW−14 IBL
```

– 6 is SS RW–14 sHLC
– 7 is Ti RW–14 IBL
– 8 is Ti RW–14 sHLC
– 9 is Swagelok 1/4"
Tube :

In this main file it is also possible to choose which graphs have to be shown or saved: 0 means no graphs, 1 show this graphs, 2 show and save the graphs, 3 save and close the graphs. To run a simulations of a certain tube the file: $co2\_simulation\_setup.m$ has to be filled and option 5has to be chosen as program.

B.1.1 Graphs

Modifications to the graphs layout can be made in $set\_graphs.m$.

Appendix C

Overview measurements

This appendix presents the characteristics of the tubes used to determine the heat transfer coefficient of CO_2. Furthermore, in section C.3 an overview of the used mass flow, saturation temperature and applied heat at which measurements have been taken place can be found.

C.1 Stave properties

Properties	IBL stave
Tube's material	Ti
Stave's material	Carbon Foam
Inner Diameter $[mm]$	2.0
Outer Diameter $[mm]$	2.2
Resistance $[\Omega]$	20.5
Length tube $[m]$	0.85
# Resistors	16
Length resistor $[m]$	0.04
Width resistor $[m]$	0.02
Thermal cond. $[Wm^{-1}\,^{\circ}K^{-1}]$	21.9
$\alpha\ [^{\circ}K^{-1}]$	$4.0 \cdot 10^{-3}$

Table C.1: Characteristics of the IBL prototype stave.

C.2   Tube properties

Properties	SS RW-12	SS RW-14	Ti RW-14	SS Swagelok
Inner Diameter $[mm]$	2.16	1.6	1.6	4.57
Outer Diameter $[mm]$	2.77	2.16	2.16	6.35
Resistance $[\Omega]$	0.479	0.799	0.602	0.119
Length tube $[m]$	1.525	1.525	1.524	1.550
Length resistor $[m]$	1.50	1.50	1.50	1.500
Therm. cond. $[Wm^{-1}\,{}^{\circ}K^{-1}]$	16.3	16.3	21.9	9.4
$\alpha\ [^{\circ}K^{-1}]$	$9.0 \cdot 10^{-4}$	$9.0 \cdot 10^{-4}$	$3.5 \cdot 10^{-3}$	$9.0 \cdot 10^{-4}$

Table C.2: Characteristics of the tubes used to determine the heat transfer coefficient of CO_2. SS implies a stainless steel tube, while Ti means that the tube is made out of titanium. The first three tubes are order from New England Small Tube [27], while the last tube is order from Swagelok [28].

C.3   Measurement Characteristics

C.3.1   SS RW-12

#	$\mathbf{T}_{sat}\ [^{\circ}C]$	Mass flow $[g/s]$ (Massflux $[kg/m^2s]$)	Applied heat $[W]$
1	-25	1.89 (515.78)	34.29, 77.18, 137.02, 173, 7, 177.23
2	-30	1.8 (518.51)	77.55, 137.82, 167.58, 309.6, 363.33, 420.38
3	-36	1.89 (491.22)	77.93, 138.31, 216.61, 261.55, 311.26
4	-18.5	1.5 (515.78)	76.43, 136.02
5	-28	1.35 (409.35)	53.26, 104.82, 172.92, 213.61, 257.83
6	-35	1.35 (368.41)	53.27, 105.52, 168.15, 215.11, 259.62
7	-26	1.35 (368.41)	52.82, 103.77, 163
8	-23	1.35 (368.41)	52.7, 103.85, 171.22, 211.49, 255.23
9	-42	1.5 (409.35)	53.95, 106.32, 175.27, 216.49

Table C.3: Experimental values of the heat transfer coefficient measurements on the SS RW-12 tube. Values are the aimed saturation temperature, the average mass flow and the total applied heat.

C.3.2   SS RW-14

#	T_{sat} [$^\circ C$]	Mass flow [g/s] (Massflux [kg/m^2s])	Applied heat [W]
1	−35	1.6 (795.77)	83.65, 130.95, 188.26, 255.76, 334.1, 376.86
2	−18	1.25 (621.70)	46.05, 81.85, 128.19, 184.2, 250.34, 325.91
3	−25	1.5 (746.04)	46.65, 82.75, 129.56, 186.3, 253.31, 330.9
4	−30	1.45 (721.17)	46.6, 83.25, 130.32, 187.36, 254.71, 277.59
5	−35	1.0 (497.36)	83.75, 131.07, 187.96, 256.29, 333.3
6	−20	1.3 (646.57)	81.85, 128.44, 184.66, 250.86
7	−28	1.4 (696.30)	81.65, 129.44, 186.3, 253.14
8	44	1.0 (497.36)	47.55, 84.35, 131.95, 189.3, 257.3

Table C.4: Experimental values of the heat transfer coefficient measurements on the SS RW-14 tube. Values are the aimed saturation temperature, the average mass flow and the total applied heat.

C.3.3   Ti RW-14

#	T_{sat} [$^\circ C$]	Mass flow [g/s] (Massflux [kg/m^2s])	Applied heat [W]
1	−26	2.0 (994.72)	82.08, 124.72, 185.5, 195.39
2	−30	1.3 (646.57)	70.73, 96.67, 126.12, 159.75, 183.97, 192.17
3	−25	1.55 (770.91)	69.08, 108.29, 155.59, 198.02
4	−30.4	1.55 (770.91)	70.58, 110.44, 158.97, 193.93

Table C.5: Experimental values of the heat transfer coefficient measurements on the Ti RW-14 tube. Values are the aimed saturation temperature, the average mass flow and the total applied heat.

C.3.4   Swagelok

#	T_{sat} [$^\circ C$]	Mass flow [g/s] (Massflux [kg/m^2s])	Applied heat [W]
1	−32	4.0 (243.65)	95.37, 157.28, 234.38, 324.18
2	−28	2.4 (146.32)	94.98, 156.55, 233.07, 325.18

Table C.6: Experimental values of the heat transfer coefficient measurements on the Swagelok tube. Values are the aimed saturation temperature, the average mass flow and the total applied heat.

Appendix D

Error propagation

D.1 Error propagation

When using multiple sensors to determine one specific value, error propagation is a necessary tool. The two research parts of this thesis are to determine the thermal impedance of Carbon Foam staves and the CO_2 heat transfer coefficient in small diameter tubes. Both values are measured indirectly as explained in chapter 3.

The GaussMarkov theorem, which is used in many textbooks and on universities [29][30] is, in general form, presented in Equation D.1 and is the bases of the error propagation used in this thesis calculations. Although most errors are systematic this theory can still be used because a large number of flat systematic errors result in a statistical prediction of the final value when they are combined.

$$\sigma_f^2 = \sum_i \left(\frac{df(x_i)}{dx_i} \right)^2 \sigma_i^2 \tag{D.1}$$

D.2 Error overview

An overview of the sensors including there errors is presented in Table D.1, while other relevant errors are presented in Table D.2.

Sensors	Error
Absolute pressure sensors	$\pm 0.2\%$ FS
Chiller	$\pm 0.1\,°\mathrm{C}$
Flow meter	$\pm 0.10\%$
Gauge pressure sensors	< 0.7 bar: 0.15% FS, > 0.7 bar: 0.05% FS
Power supply (applying heat)	$0.035\% + 40$ mV, $0.2\% + 85$ mA
Temperature sensors	$\pm(0.15 + 0.002T)$

Table D.1: Overview of used electronic device that have relevant errors, with FS full scale and T the temperature $[°C]$.

Value	Error (σ^2)
Inner diameter tube (D_i)	$\sigma_{D_i}^2 = (0.01 \cdot D_i)^2$
Length tube (L_t)	$\sigma_{L_t}^2 = (0.01 \cdot L)^2$
Outer diameter tube (D_i)	$\sigma_{D_i}^2 = (0.01 \cdot D_i)^2$
Resistance tube (R_{ohm})	$\sigma_{R_{ohm}}^2 = (0.004 \cdot R_0)^2$
Width stave (W_t)	$\sigma_{W_t}^2 = (0.01 \cdot W)^2$

Table D.2: Overview of relevant errors.

D.2.1 Thermal Impedance

To determine the error in the calculated thermal impedance R, first the errors in all the intermediate step have to be calculated. In this section this is done starting with the error calculation in the thermal impedance and ending with the known errors.

The error in the thermal impedance is formulated in Equation D.2,

$$\sigma_R^2 = \left(\frac{1}{q}\right)^2 \sigma_{\Delta T_{s-w}}^2 + \left(\frac{\Delta T_{s-w}}{q^2}\right)^2 \sigma_q^2 \tag{D.2}$$

with σ_q^2 as in Equation D.3 and $\sigma_{\Delta T_{s-w}}^2$ as in Equation D.4.

$$\sigma_{\Delta T_{s,w}}^2 = \sigma_{T_s}^2 + \sigma_{T_w}^2 + \sigma_{T_{fluid}}^2 \tag{D.3}$$

$$\sigma_q^2 = \left(\frac{1}{l \cdot w}\right)^2 \sigma_Q^2 + \left(\frac{Q}{l^2 \cdot w}\right)^2 \sigma_l^2 + \left(\frac{1}{l \cdot w^2}\right)^2 \sigma_w^2 \tag{D.4}$$

Here σ_Q^2 is formulated as Equation D.5.

$$\sigma_Q^2 = (2IR_{ohm})^2 \sigma_I^2 + \left(I^2\right)^2 \sigma_{R_{ohm}}^2 \tag{D.5}$$

D.2.2 Heat Transfer Coefficient

The error in the heat transfer coefficient is formulated in Equation D.6,

$$\sigma_h^2 = \left(\frac{1}{\pi D_i l \Delta T_{w,f}}\right)^2 \cdot \left[\sigma_Q^2 + \left(\frac{Q}{\Delta T_{w,f}}\right)^2 \sigma_{T_{w,f}}^2 + \left(\frac{Q}{D_i}\right)^2 \sigma_{D_i}^2 + \left(\frac{Q}{l}\right)^2 \sigma_l^2\right] \tag{D.6}$$

with σ_Q^2 as in Equation D.5, $\sigma_{D_1}^2$ and σ_l^2 as in Table D.2 and $\sigma_{\Delta T_{w,f}}^2$ as in Equation D.7.

$$\sigma_{\Delta T_{w,f}}^2 = \sigma_{T_s}^2 + \sigma_{T_{fluid}}^2 \tag{D.7}$$

D.2.3 Vapor Quality

The calculation of the error in the vapor quality is more extended than the two former ones, therefore only the final result is shown in Equation D.8.

$$\sigma_\chi^2 = \sigma_{\chi_{inlet}}^2 + \left(\frac{1}{\dot{m}}\right)^2 \sigma_Q^2 + \left(\frac{Q}{\dot{m}^2}\right)^2 \sigma_{\dot{m}}^2 \tag{D.8}$$

with $\sigma^2_{\chi_{inlet}}$ as in Equation D.9, σ^2_Q as in Equation D.5 and $\sigma^2_{\dot{m}}$ as in Table D.1.

$$\sigma^2_{\chi_{in}} = 2 \left(\frac{1}{\Delta E} \right)^2 \sigma^2_{E_{in}} + \left(\frac{E_{in} - E}{\Delta E^2} \right)^2 \sigma^2_{\Delta E} \tag{D.9}$$

Here E the enthalpy $[kJ/m^2]$, ΔE the enthalpy difference between vapor quality 0 and 1, and E_{in} the corresponding value of enthalpy belonging to the vapor quality that enters the tube. The enthalpy is read out from the NIST database when the temperature and pressure of the fluid is known, therefore the errors are: $\sigma^2_{E_{in}} \leq 2$ and $\sigma^2_{\Delta E} \leq 4$.

Appendix E

Labview

The data acquisition for the setup is done with National Instruments devices and labVIEW software. A NI cDAQ 9172 with 8 slots is the main box. One NI 9205 unit and seven NI 9217 units are plugged in. The former is used to read out the pressure sensors and mass flow, the latter is used to read out up to 28 temperature sensors.
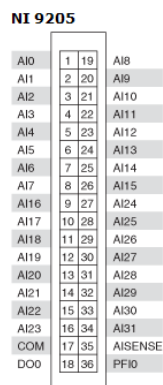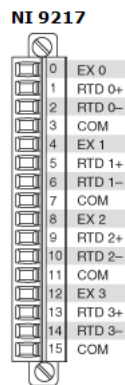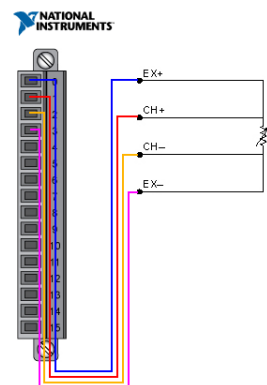
E.1   NI device

Figure E.1

Figure E.2

Figure E.3

NI instr	NI Mod - CH	#	Sensor	Place	Type
NI 9205	I - ai0	0	Temperature [$°C$]	Mass/Flow	Current
NI 9205	I - ai1	1	Mass [g/s]	Mass/Flow	Current
NI 9205	I - ai2	2	Ground	Not in use	Voltage
NI 9205	I - ai3	3	Ground	Not in use	Voltage
NI 9205	I - ai4	4	Pressure [Bar]	Pre-Hexx	Current
NI 9205	I - ai5	5	Pressure [Bar]	Pre-Buck	Current
NI 9205	I - ai6	6	Humidity [%]	Voltage	Voltage
NI 9205	I - ai7	7	Pressure [Bar]	P in	Voltage
NI 9205	I - ai16	8	Pressure [Bar]	P out	Voltage
NI 9205	I - ai17	9	Ground	Not in use	Voltage
NI 9205	I - ai18	10	Ground	Not in use	Voltage
NI 9205	I - ai19	11	Not in use	Not in use	-
NI 9205	I - ai20	12	Not in use	Not in use	-
NI 9205	I - ai21	13	Not in use	Not in use	-
NI 9205	I - ai22	14	Not in use	Not in use	-
NI 9205	I - ai23	15	Not in use	Not in use	-
NI 9217	II - ai0:ai3	16	Temperature [$°C$]	T Ambient I	Voltage
NI 9217	II - ai4:ai7	17	Temperature [$°C$]	T Pre-Needle	Voltage
NI 9217	II - ai8:ai11	18	Temperature [$°C$]	T in	Voltage
NI 9217	II - ai12:ai15	19	Temperature [$°C$]	T out	Voltage
NI 9217	III - ai0:ai3	20	Temperature [$°C$]	T1	Voltage
NI 9217	III - ai4:ai7	21	Temperature [$°C$]	T2	Voltage
NI 9217	III - ai8:ai11	22	Temperature [$°C$]	T3	Voltage
NI 9217	III - ai12:ai15	23	Temperature [$°C$]	T4	Voltage
NI 9217	IV- ai0:ai3	24	Temperature [$°C$]	T5	Voltage
NI 9217	IV - ai4:ai7	25	Temperature [$°C$]	T6	Voltage
NI 9217	IV - ai8:ai11	26	Temperature [$°C$]	T7	Voltage
NI 9217	IV - ai12:ai15	27	Temperature [$°C$]	T8	Voltage
NI 9217	V - ai0:ai3	28	Temperature [$°C$]	T9	Voltage
NI 9217	V - ai4:ai7	29	Temperature [$°C$]	T10	Voltage
NI 9217	V - ai8:ai11	30	Temperature [$°C$]	T11	Voltage
NI 9217	V - ai12:ai15	31	Temperature [$°C$]	T12	Voltage
NI 9217	VI - ai0:ai3	32	Temperature [$°C$]	T13	Voltage
NI 9217	VI - ai4:ai7	33	Temperature [$°C$]	T14	Voltage
NI 9217	VI - ai8:ai11	34	Temperature [$°C$]	T15	Voltage
NI 9217	VI - ai12:ai15	35	Temperature [$°C$]	T16	Voltage
NI 9217	VII - ai0:ai3	36	Temperature [$°C$]	T17	Voltage
NI 9217	VII - ai4:ai7	37	Temperature [$°C$]	T18	Voltage
NI 9217	VII - ai8:ai11	38	Temperature [$°C$]	T19	Voltage
NI 9217	VII - ai12:ai15	39	Temperature [$°C$]	T20	Voltage
NI 9217	VIII - ai0:ai3	40	Temperature [$°C$]	T21	Voltage
NI 9217	VIII - ai4:ai7	41	Temperature [$°C$]	T22	Voltage
NI 9217	VIII - ai8:ai11	42	Temperature [$°C$]	T23	Voltage
NI 9217	VIII - ai12:ai15	43	Temperature [$°C$]	T24	Voltage

Table E.1: Connection table with location and purpose of used sensors that are connected to the NI device and are read-out by the Labview program.

Appendix F

Sensors

Sensors	Model	Range
Absolute pressure sensors	PTX 7200	0 to 1400 bar
Chiller	PolyScience 6561T	-10 to 35 °C max. 2.9 kW
CO_2 bottle	Airgas	50 lb
Flow meter	Rheonik RHM 015	0.004 to 0.6 kg/min
Gauge pressure sensors	Druck DPI 104	0 to 690 bar
Humidity sensors	Apollo HIH series	0 to 100% RH
Labview DAQ	NI c-DAG 9172	8 blocks
Labview blocks	NI 9205 & NI9217	All & RTD sensors, resp.
Power supply (applying heat)	Agilent 6032A	20V, 50A
Power supply (electronics)	BK precision 1786A	0 to 30V
Safety sensors	Therm Coil TD1 2754K	60 to 250 °F
Temperature sensors	OmegaFilm Pt Class A	-50 to 450 °C

Table F.1: Overview of used electronic device and sensors.

Appendix G

Wires